Electronic Supplementary Material (ESI) for ChemComm.

Supporting Information

Engineering Zirconium-based UiO-66 for Effective Chemical Conversion of D-Xylose to Lactic Acid in Aqueous Condition

Panyapat Ponchai,[a] Kanyaporn Adpakpang,[a] Sutarat Thongratkaew,[b] Kawisa Chaipojjana,[b] Suttipong Wannapaiboon,[c] Siwarut Siwaipram,[a] Kajornsak Faungnawakij,[b] and Sareeya Bureekaew*[a,d]

[a.] School of Energy Science and Engineering, Vidyasirimedhi Institute of Science and Technology, 555 Moo 1 Payupnai, Wangchan, Rayong 21210, Thailand.

[b.] National Nanotechnology Center (NANOTEC), National Science and Technology Development Agency (NSTDA), 111 Thailand Science Park, Pahonyothin Rd., Klong Luang, Pathumthani 12120, Thailand.

[c.] Synchrotron Light Research Institute, 111 University Avenue, Muang, Nakhon Ratchasima 30000, Thailand.

[d.] Research Network of NANOTEC-VISTEC on Nanotechnology for Energy, Vidyasirimedhi Institute of Science and Technology, Wangchan, Rayong, 21210, Thailand

Experimental Section

Synthesis of UiO-66, UiO-66(AA), and UiO-66(AA)*. UiO-66 was prepared by following the reported procedure with some modifications.[1] Typically, 0.159 g of zirconium(IV) chloride ($ZrCl_4$, Sigma-Aldrich), 0.102 g of 1,4-benzenedicarboxylic acid (H_2BDC, Sigma-Aldrich), and 25 ml of N,N-dimethylformamide (DMF, Daejung) were mixed in the 100 mL screw-cap bottle and then heated at 120 °C for 24 h in an oven. UiO-66(AA) was prepared according to the previous report.[2] In brief, 0.180 g of $ZrCl_4$ and 0.128 g of H_2BDC were dissolved in 40 ml of DMF and stirred for 20 min. Then, 5 ml of glacial acetic acid (AA, Sigma-Aldrich) was added, and the mixture was stirred further for 10 min and heated at 120 °C for 24 h. The resulting white powders of UiO-66 and UiO-66(AA) were collected by centrifugation. After that, they were washed three times with DMF and ethanol and then dried in a vacuum oven at room temperature for 12 h. UiO-66(AA)* is prepared by refluxing UiO-66(AA) with DI 100 mL at 120°C-3h for 3 times.

Material Characterization. The crystalline phase and crystallinity of the synthesized samples were examined using powder X-ray diffraction (PXRD) analysis (Cu Kα radiation (λ = 1.54 Å), Bruker, New D8 Advance). Thermogravimetric analysis (TGA) measurement was performed under nitrogen atmosphere at the flow rate of 100 $cm^3\ min^{-1}$ with the ramping rate of 10 $°C\ min^{-1}$ by using Rigaku thermal plus evo2 (TG 8121). The morphology and particle size were analyzed with a field-emission scanning electron microscope (FE-SEM, JEOL, JSM-7610F). Nitrogen adsorption-desorption isotherms were recorded at 77 K using Bel-Max sorption analyzer. Before the measurements, the samples were activated at 200 °C under evacuation for 3 h to eliminate all guest molecules. Zr K-edge EXAFS measurement was performed at the BL1.1W: Multiple X-ray Techniques Beamline, Synchrotron Light Research Institute, Thailand. The measurement was conducted at ambient temperature and pressure by simultaneously measuring the samples together with the Zr foil as a standard reference for an in-line alignment of the energy shift during the synchrotron-operating time. The data processing, *i.e.* normalization and fitting was performed using ATHENA and ARTEMIS software.[3]

Lactic acid production. The LA production was conducted in the 80 ml Teflon-lined stainless-steel autoclave reactor equipped with a thermocouple. 0.45 g of D-xylose (Acros organics) was dissolved in 30 ml of DI water and charged into the reactor. Then, 0.25 g of catalyst was added. The batch reactions were performed in an inert atmosphere (N_2, 15 bar) under a constant agitation of 300 rpm. The reactions were conducted at various temperatures and reaction times to find out the optimal condition. Experiments on the catalytic activity using the commercial ZrO_2 and ZnO (CARLO ERBA reagents) were also performed and used to compare with those of the synthesized UiO-66 products. After the reaction, the reactor was cooled down to room temperature in an ice-water bath. The liquid phase was filtered prior to analyzing by high-performance liquid chromatography (HPLC, Shimadzu) equipped with both a UV detector adjusted to 210 nm and a refractive index (RI) detector using Hiplex-H column (300 mm in length with a 7.7 mm i.d.; Agilent Technologies, USA). The column temperature was set to 45 °C. The samples were eluted by 8.5 mM sulfuric acid (aq.) at the constant flow rate of 0.6 $mL\ min^{-1}$. The catalyst performances were evaluated in terms of D-xylose conversion calculated based on a molar basis as follows:

$$Conversion = \frac{[Xylose]_{initial} - [Xylose]_{final}}{[Xylose]_{initial}} * 100$$

$$Yield = \frac{[Mole\ of\ Product]}{[Mole\ of\ Xylose_{initial}]} \times 100$$

Quantitative analysis of each component was accomplished using calibration curves of commercially available DL-lactic acid, formic acid, acetic acid and furfural.

Theoretical simulation. All theoretical calculations were performed using Gaussian 09 program package. Density functional theory (DFT) M06-L functional was employed.[4] LANL2DZ basis set with pseudopotential[5] was used for Zr atoms and Dunning/Huzinaga full double zeta basis set (D95)[6] was used for the remaining atoms. The model of $Zr_6O_4(OH)_5(formate)_{11}$ for the catalyst was used in the calculation. Defective Zr centers, which are considered as the active sites, coordinate with hydroxyl group (–OH) and water. During geometry optimization, no atoms were constrained. Frequency calculations were performed at the same level of theory to verify the transition state. Additionally, the intrinsic reaction coordination (IRC) was calculated to ensure that the transition state leads to the reactant and products of interest.

Table S1. Summary of the catalytic performance of UiO-66 catalyst for 4 h at various reaction temperatures.

Reaction temperature (°C)	D-Xylose conversion (%)	Lactic acid yield (mol/1 mol D-xylose)	Furfural yield (mol/1 mol D-xylose)	Carbon balance
150	89.90 ± 0.36	0.79 ± 0.03	0.19 ± 0.01	0.74
170	98.26 ± 0.32	1.17 ± 0.04	0.20 ± 0.01	0.91
190	98.77 ± 0.13	0.83 ± 0.01	0.12 ± 0.01	0.62

Table S2. Summary of the catalytic performance of UiO-66 for 170°C at various reaction times.

Reaction time (h)	D-Xylose conversion (%)	Lactic acid yield (mol/1 mol D-xylose)	Furfural yield (mol/1 mol D-xylose)	Carbon balance
0.5	88.83 ± 1.95	0.60 ± 0.07	0.15 ± 0.03	0.57
1	89.91 ± 0.71	0.71 ± 0.03	0.19 ± 0.00	0.68
2	94.64 ± 0.59	0.95 ± 0.01	0.21 ± 0.00	0.82
4	98.26 ± 0.32	1.17 ± 0.04	0.20 ± 0.01	0.91
6	98.38 ± 0.32	1.05 ± 0.09	0.19 ± 0.01	0.83
12	98.95 ± 0.10	0.90 ± 0.08	0.11 ± 0.02	0.66
24	99.06 ± 0.02	0.59 ± 0.04	0.06 ± 0.00	0.42

Table S3. Summary of catalytic performance by different catalysts for D-xylose conversion at 170°C 4h.

Catalyst	D-Xylose conversion (%)	Lactic acid yield (mol/1 mol D-xylose)	Furfural yield (mol/1 mol D-xylose)	Carbon balance
No-catalyst	52.94 ± 1.23	0.03 ± 0.01	0.37 ± 0.00	0.72
ZrO_2	77.84 ± 4.82	0.55 ± 0.03	0.40 ± 0.02	0.94
ZnO	99.55 ± 0.28	0.45 ± 0.02	0.04 ± 0.00	0.31
UiO-66	98.26 ± 0.32	1.17 ± 0.04	0.20 ± 0.01	0.91
UiO-66(AA)	98.50 ± 0.26	0.76 ± 0.00	0.09 ± 0.00	0.56
UiO-66(AA)*	98.00 ± 0.10	1.14 ± 0.01	0.13 ± 0.00	0.83

Table S4. Summary of catalytic performance and recyclability of UiO-66 for D-xylose conversion.

No. of recycle	D-Xylose conversion (%)	Lactic acid yield (mol/1 mol D-xylose)	Furfural yield (mol/1 mol D-xylose)	Carbon balance
1	98.26 ± 0.32	1.17 ± 0.04	0.20 ± 0.01	0.91
2	97.35 ± 2.10	0.72 ± 0.03	0.38 ± 0.04	0.83
3	95.22 ± 0.08	0.50 ± 0.01	0.46 ± 0.01	0.81

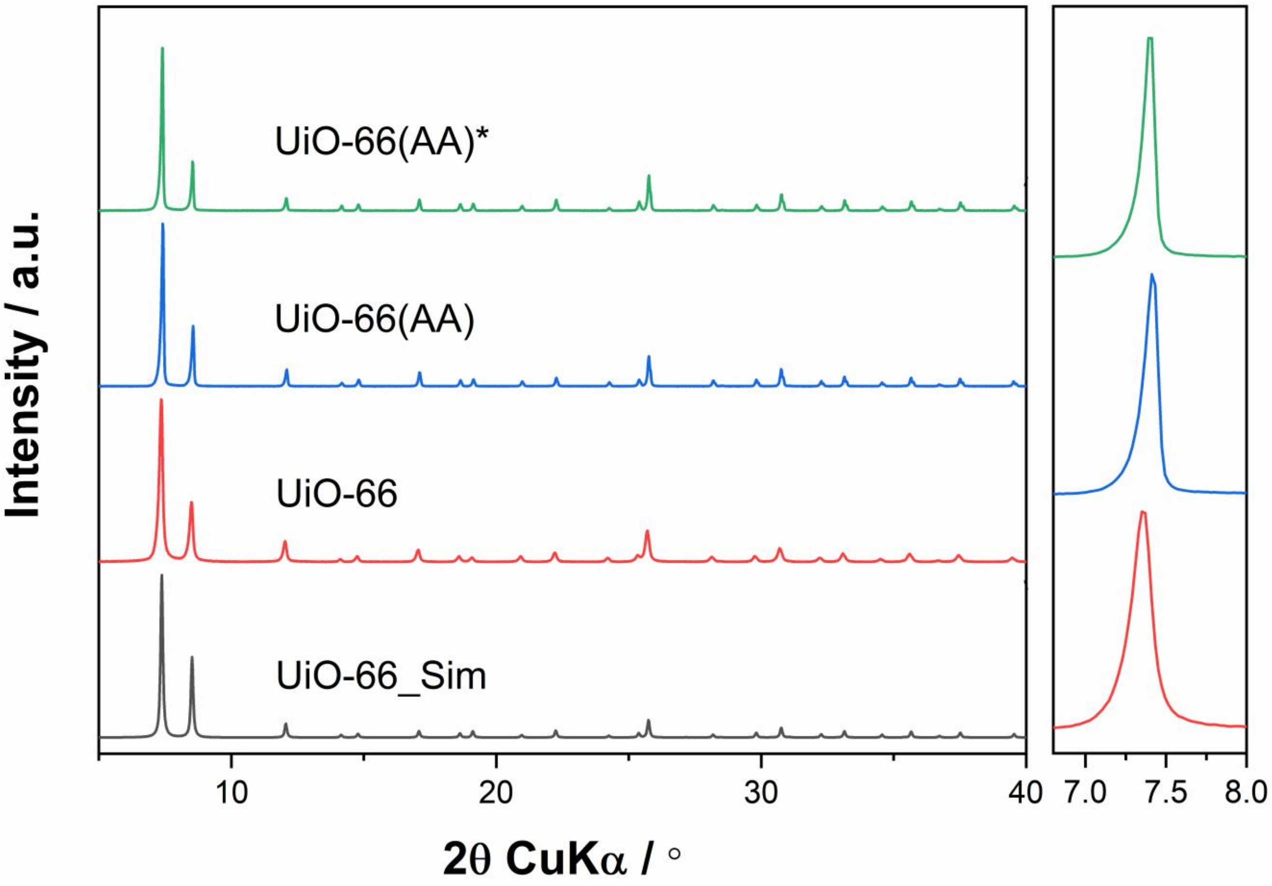

Figure S1. PXRD patterns of UiO-66, UiO-66(AA), UiO-66(AA)* and the simulation of UiO-66, respectively.

：Compared with UiO-66, UiO-66(AA) presents narrower full width at half maximum of the major peak suggesting the higher crystallinity and larger crystallite site of the particle. Additionally, the width does not change upon the refluxing with DI water (UiO-66(AA)*) indicating the remained high crystallinity.

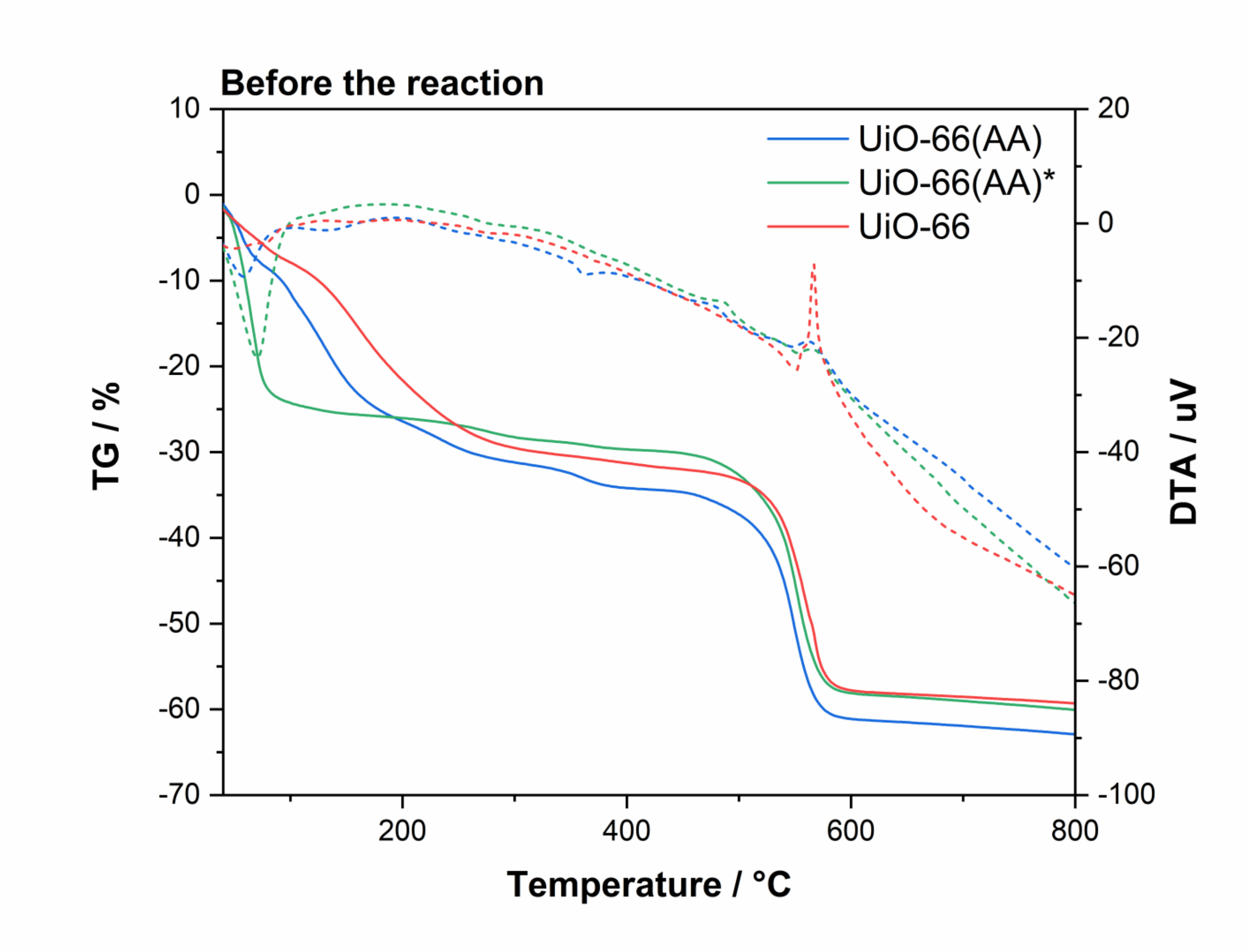

Figure S2. TGA (solid line) and DTA (dotted line) curves of as-synthesized UiO-66 (red), UiO-66(AA) (blue), and UiO-66(AA)* (green) measured under N_2.

: All catalysts show high thermal stability up to 450 °C which is beneficial for the LA production under hydrothermal reaction at elevated temperature.

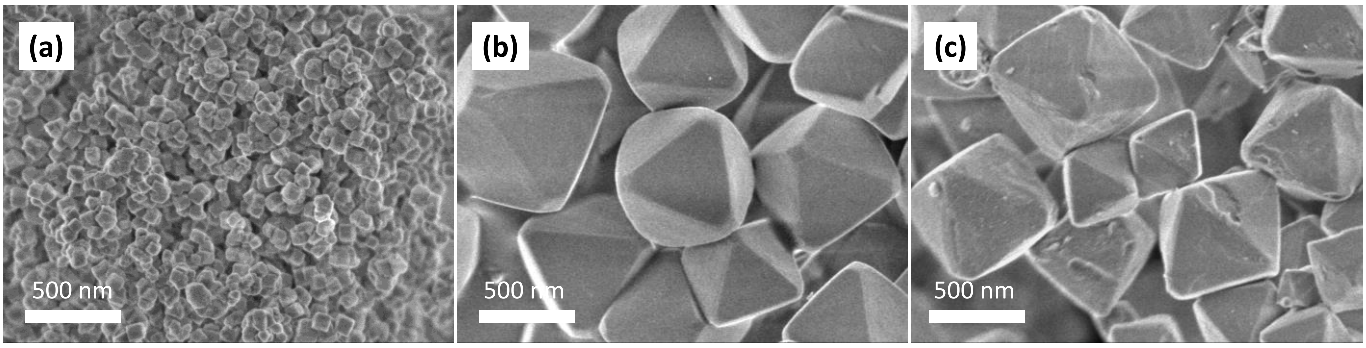

Figure S3. SEM images of the synthesized (a) agglomerated cube UiO-66, (b) octahedral UiO-66(AA) and (c) octahedral UiO-66(AA)*, respectively.

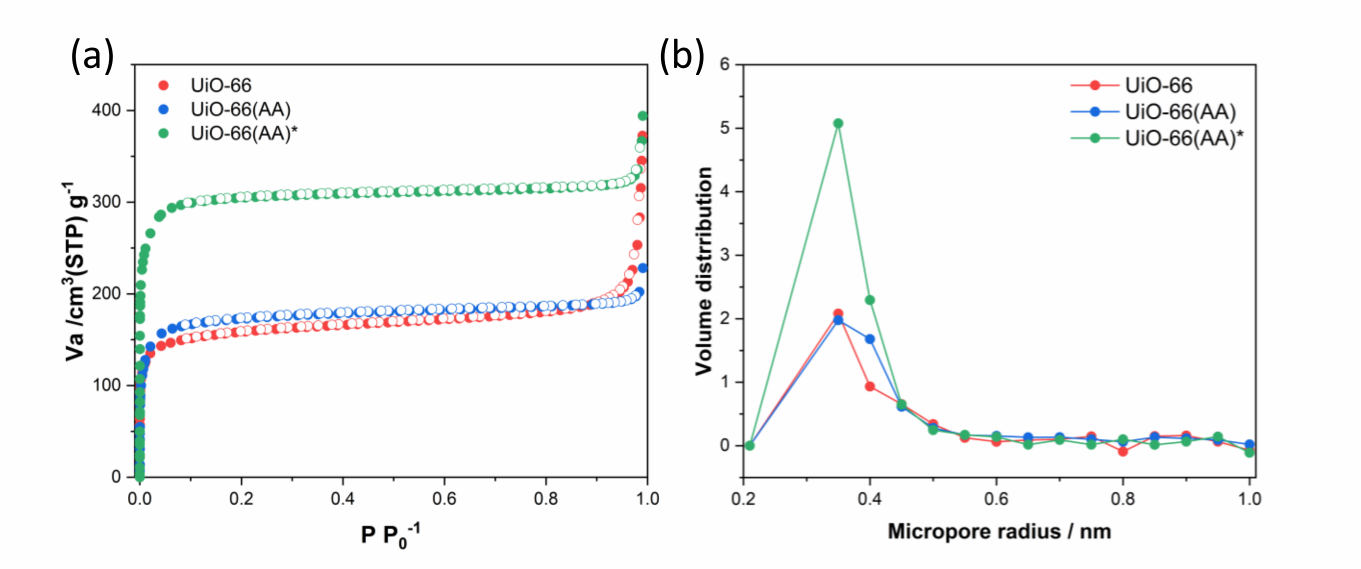

Figure S4. N_2 sorption isotherms and pore size distributions of the UiO-66, UiO-66(AA), and UiO-66(AA)* measured at 77 K. Filled and opened circles represent adsorption and desorption, respectively.

: After refluxing with DI water, pore volume and surface area of UiO-66(AA)* significantly increase.

Table S5. Summary of N_2 sorption capacities of the UiO-66, UiO-66(AA), and UiO-66(AA)* measured at 77 K. Their surface areas and pore volumes were calculated based on the Brunauer–Emmett–Teller (BET) and t-plot analysis.

Sample	Specific surface area (m^2 g^{-1})	Micropore volume (cm^3 g^{-1})
UiO-66	601.17	0.2264
UiO-66(AA)	669.71	0.2614
UiO-66(AA)*	1,198.80	0.4642

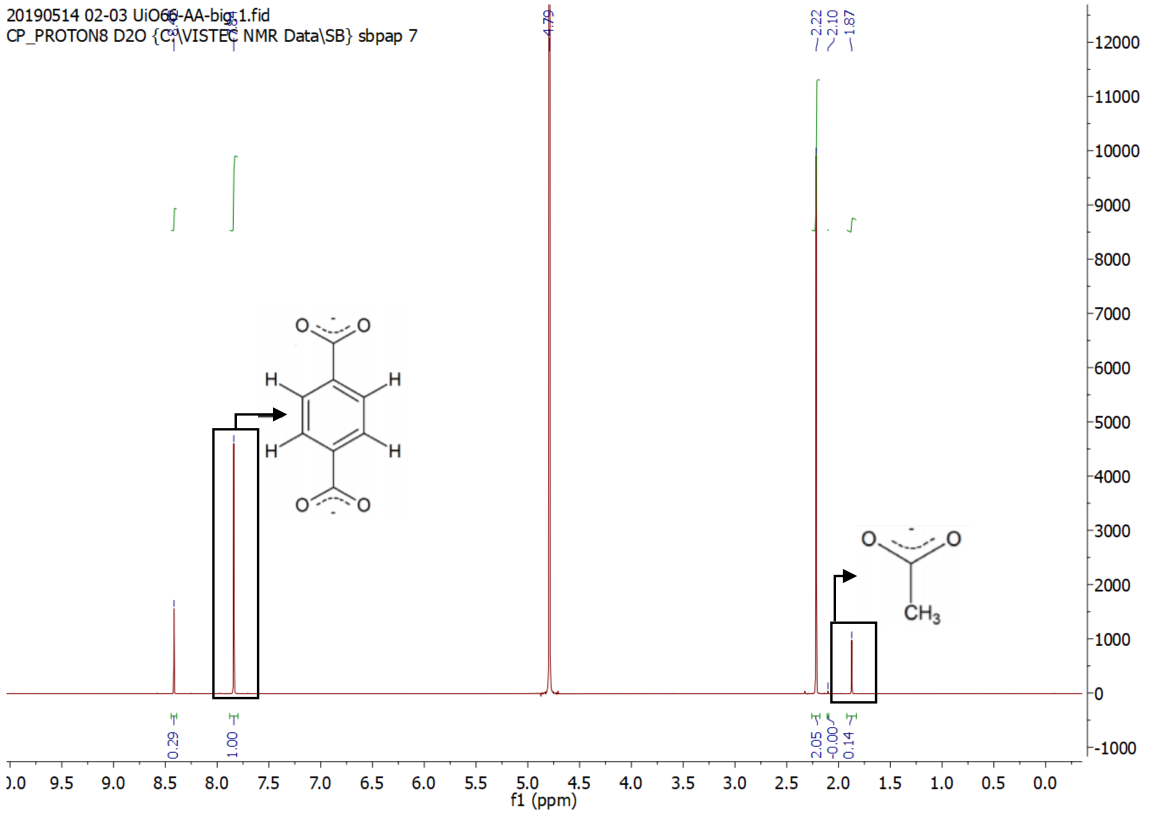

Figure S5. NMR spectrum of UiO-66 in D_2O solvent digested by NaOH.

$$\frac{\mathrm{AA}}{\mathrm{BDC}}\mathrm{m_R} = \left(\frac{\mathrm{AA\ 1H\ Int.}}{\mathrm{N_{H(AA)}}}\right) \times \left(\frac{\mathrm{N_{H(BDC)}}}{\mathrm{BDC\ 1H\ Int.}}\right) = \left(\frac{\mathrm{AA\ 1H\ Int.}}{3}\right) \times \left(\frac{4}{\mathrm{BDC\ 1H\ Int.}}\right)$$

Table S6. Summary of molar ratio of AA/BDC in the MOF catalysts.

Sample	AA/BDC
UiO-66	-
UiO-66(AA)	0.32
UiO-66(AA)-post reaction	0.07
UiO-66(AA)-refluxing DI (1st)	0.15
UiO-66(AA)-refluxing DI (2nd)	0.08
UiO-66(AA)-refluxing DI (3rd)	0.08
UiO-66(AA)*	0.08

Refluxing conditions: 120°C-3h in DI water.

: The fresh UiO-66(AA) shows a high AA:BDC ratio of 0.32 while the used catalyst possesses the ratio of 0.07. The high concentration of AA in the fresh UiO-66(AA) is due to both Zr-coordinated AA at the defects and AA inside the pore as a guest molecule. Substantial reduction of AA after the reaction indicates the de-coordination of AA from the defects. Accordingly, the additional catalytic sites from AA-leaching can be generated during the reaction to convert D-xylose to LA.

Taking into account that all the catalysts delivered comparable D-xylose conversion over 98 %, the incorporated AA has no significant effect to the D-xylose conversion. Instead, the LA yield is mainly affected by the coordinated AA, which is directly related to the accessible Lewis acid catalytic site. When the UiO-66(AA) was used, the accessible Lewis acid catalytic site was limited due to the coordinated AA, resulting in the low yield of LA. The improved LA yield was achieved from the activated UiO-66(AA)*, providing ready-to-use active sites, which required rather long refluxing time to remove the coordinated AA.

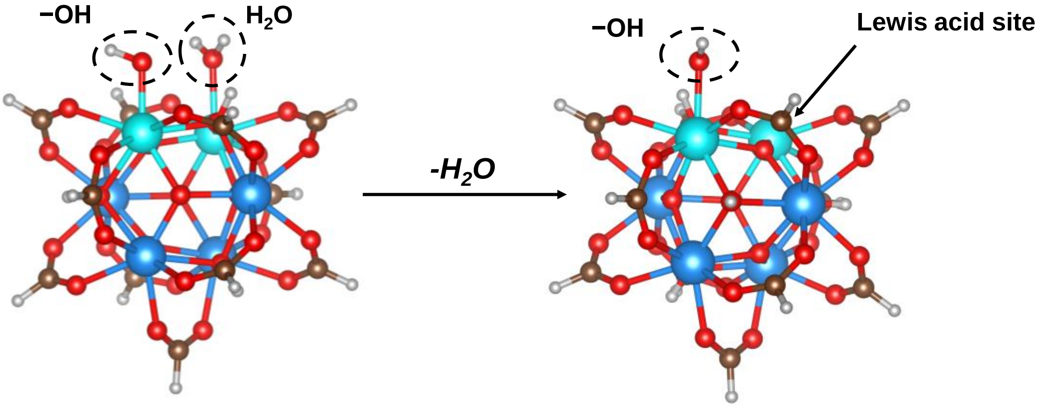

Figure S6. Structure of defective $Zr_6O_4(OH)_5(formate)_{11}{\cdot}H_2O$. The active Lewis site was obtained after the dehydration of the cluster. The accessible Zr site was employed for D-xylose conversion reaction. (color code: cyan = Zr at defective linker site, blue = non-defective Zr site, red = O, brown = C, and gray = H).

: To gain more insight into the mechanism of the conversion of D-xylose to LA by UiO-66 catalyst at a molecular level, the DFT calculations were performed. Note that the calculations were performed in gas phase without the consideration of solvent effect. A small building unit of UiO-66 with one missing linker containing 6 zirconium ions, 4 μ_3–O, 4 μ_3—OH, 11 formate, and 1 OH^- was optimized without fixing atoms. As illustrated in Figure S6, one missing carboxylate linker produces two defective Zr sites coordinated with either OH^- or H_2O. Under the hydrothermal reaction at high temperature, the coordinated H_2O can leave Zr resulting in the accessible Lewis acid Zr site.

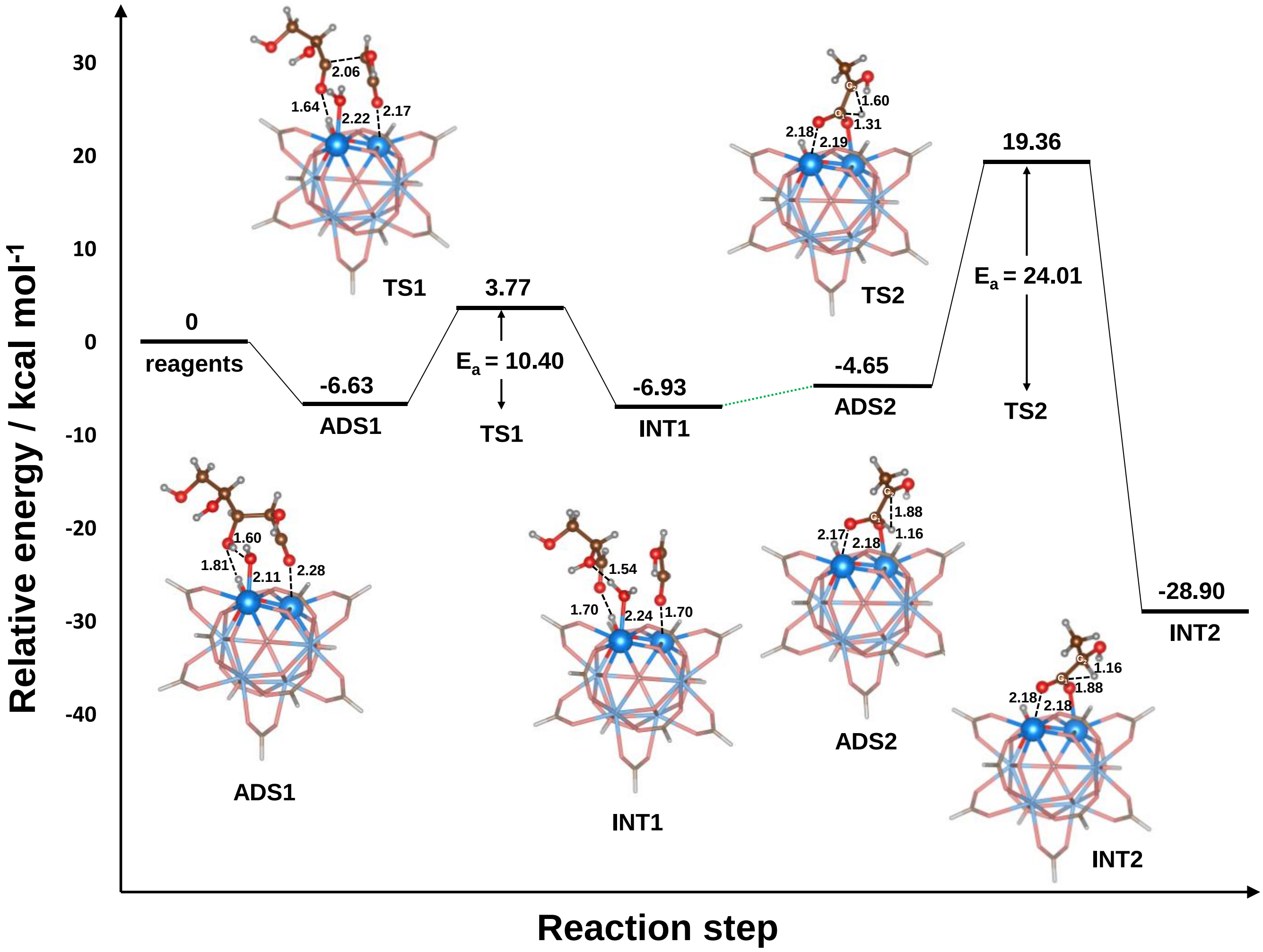

Figure S7. Reaction profile for C–C cleavage of xylose and hydride shift over the $Zr_6O_4(OH)_5(formate)_{11}$ cluster. The inserted numbers are the relative energies (ΔE) given in kcal mol^{-1}. The notations of ADS1, TS1 and INT1 refer to the adsorption, transition and intermediate states of the C–C cleavage of xylose reaction and ADS2, TS2 and INT2 refer to the adsorption, transition and intermediate steps of the hydride shift process, respectively.

: The Zr-based cluster attributes to induce and accelerate the retro-aldol condensation by a strong interaction between D-xylose molecule with hydroxyl group and Lewis acid site of Zr atom in the cluster. The probe molecule (D-xylose) is adsorbed on the Zr-based cluster stabilized by -6.63 kcal mol^{-1} with the distance of $O_{xylose}\cdots Zr_{Lewis}$ and $H_{xylose}\cdots O_{OH}$ by 2.28 Å and 1.60 Å, respectively (ADS1). Then, the C_2–C_3 cleavage of xylose proceeds with a low energy barrier of 10.40 kcal mol^{-1}. At this step, the C_2–C_3 bond of xylose is elongated from 1.60 Å to 2.06 Å (TS1). This leads to the formation of glyceraldehyde and glycolaldehyde molecules as products (INT1). Glyceraldehyde then undergoes dehydration and tautomerization to form pyruvaldehyde. Afterward, the transformation of pyruvaldehyde to LA was investigated. Our calculation shows that pyruvaldehyde molecule is adsorbed on the Zr-based cluster stabilized by -4.65 kcal mol^{-1}. The reactant interaction with the open metal site Zr atom by distance of 2.17 Å (ADS2). At the transition state, the hydroxyl group on the defective Zr attacks carbonyl resulting in H migration from the C_1 to C_2 with the activation energy of 24.01 kcal mol^{-1} (TS2). The proposed mechanism based on DFT simulation is illustrated in Figure S8.

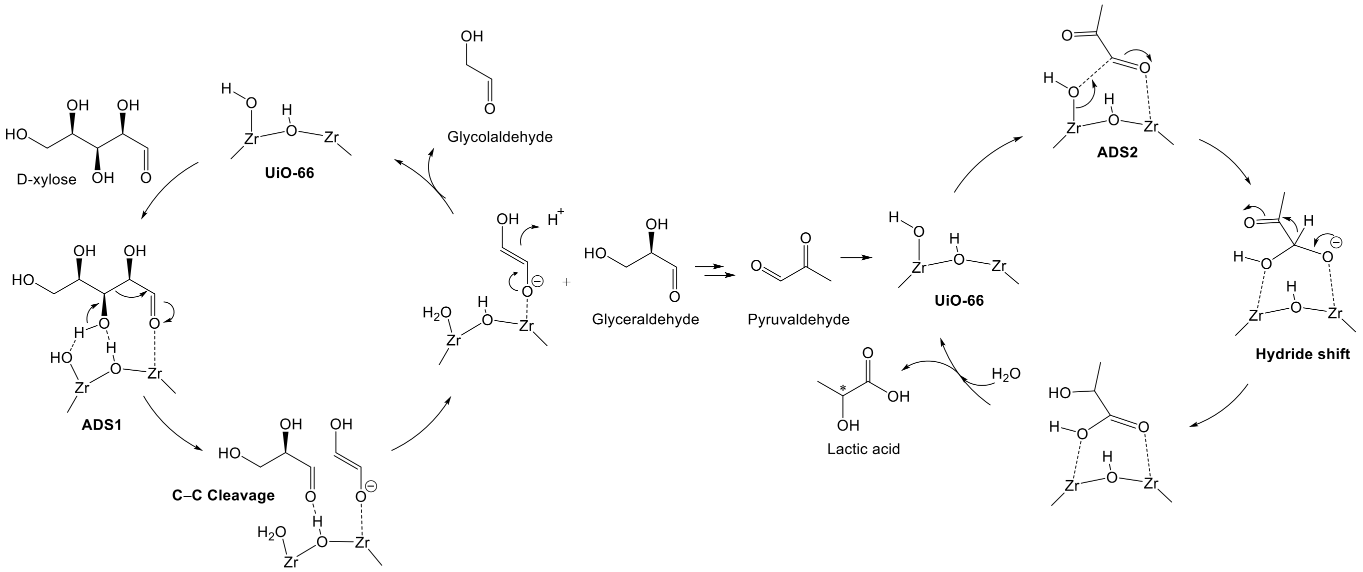

Figure S8. Proposed reaction mechanism for the conversion of D-xylose to LA with UiO-66 catalyst via retro-aldol condensation. Lewis acid (Zr^{4+}) and Zr–OH activate the carbonyl function groups facilitating C_2–C_3 cleavage and the transformation of pyruvaldehyde to LA via intramolecular rearrangement by hydride shift.

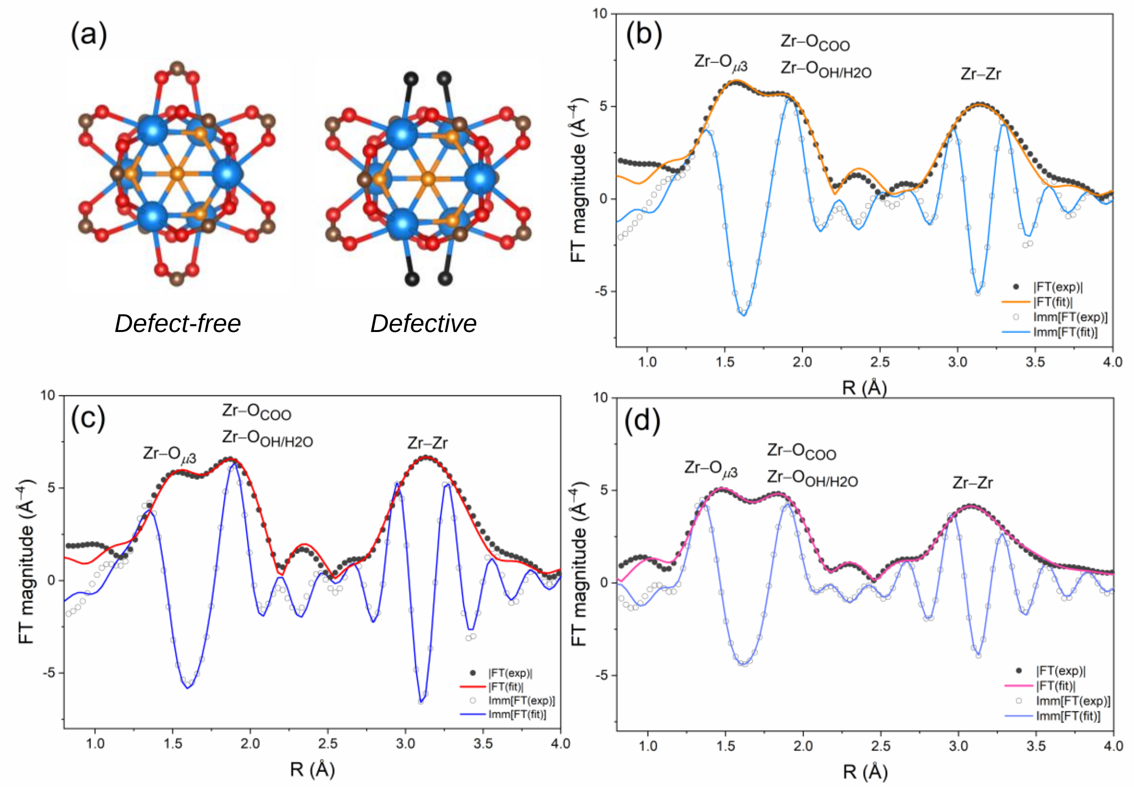

Figure S9. Illustrations of (a) defect-free and defective inorganic nodes used in the fitting, and Zr K-edge EXAFS spectra of (b) UiO-66, (c) UiO-66(AA) and (d) UiO-66(AA)*. Zr, $O_{\mu3}$, O_{COO}, and $O_{OH/H2O}$ are shown in blue, orange, red, and black, respectively. FT of k-range: 3.0 - 12.5 Å^{-1} (3.0 - 12.0 Å^{-1} for UiO-66(AA)*) using k^3-weighing. Fitting R-range: 1.15 - 4.2 Å

: To clearly explain the distinct catalytic performances of the UiO-66, UiO-66(AA), and UiO-66(AA)* based on defect concentration at the Zr nodes, Zr K-edge EXAFS analysis was employed. Zr K-edge EXAFS spectra of UiO-66, UiO-66(AA), and UiO-66(AA)* together with the model cluster were depicted in Figure S9. Typically, the first shell scattering peak from Zr atom of UiO-66 is a convolution of the scattering from nearest oxygens of the $Zr_6O_4(OH)_4$ cluster, denoted as Zr–$O_{\mu3}$, and from oxygens of BDC linker and hydroxyl group or water, denoted as Zr–O_{COO} and Zr–$O_{OH/H2O}$, respectively. Further scattering resulting in the second peak is mainly attributed to the Zr–Zr scattering.[7] As shown in Figure S9, the peak ratios of the first shell scattering from the Zr–$O_{\mu3}$ and Zr–O_{COO}/Zr–$O_{OH/H2O}$ of UiO-66, UiO-66(AA), and UiO-66(AA)* are different, suggesting their altered contribution of the defective sites. Insightful information of the bond length and numbers of defective sites were achieved by the EXAFS fitting analysis using the $Zr_6O_4(OH)_4(COO)_{11}(OH/H_2O)$ model adapted from the reported crystallographic data.[7b] A view of the model with defective local structure and the ideal local structure was depicted in Figure S9(a). The defective Zr atom is denoted as Zr(1). The defective cluster contains 2 atoms of Zr(1) with the remaining 4 atoms of defect-free Zr, denoted as Zr(2). Later, if not specified, the Zr refers to the combination of Zr(1) and Zr(2). The EXAFS fitting was performed by a typical fitting manner. The degeneracy (N) of innermost Zr–$O_{\mu3}$ shell was constrained as 4. Considering the combination of both defect-free and defective Zr-atom in the single cluster, the contribution percentage of the defective Zr–$O_{OH/H2O}$ site and the Zr–O_{COO} site was estimated for the first shell fitting based on the single degeneracy (N) manner. The resulting estimated N values of Zr(1)–$O_{OH/H2O}$/Zr(2)–O_{COO} were 0.14/0.86, 0.09/0.91 and 0.24/0.76 for UiO-66, UiO-66(AA) and UiO-66(AA)*, respectively. The dissimilar N values indicate the different numbers of defective sites in each sample. These estimated N values were employed in the further fitting. The overall spectral fitting results are illustrated in Table S7. The acceptable amplitude reduction factor ($\boldsymbol{S_0^2}$) and Debye-Waller factor (σ) were obtained, suggesting that the experimental fitting data of all the catalysts well agreed with the crystallographic data of the model. Note that the slightly large σ values of carbon and outer shell-oxygen can be attributed to their low scattering power with further distance as compared to the inner-shell oxygen and Zr. Both UiO-66 and UiO-66(AA) possess the first shell scattered Zr–$O_{\mu3}$ and Zr–O_{COO} bond lengths of *ca.* 2.11 Å and *ca.* 2.26 Å, respectively. The slight change in the Zr–$O_{\mu3}$ and Zr–O_{COO} bond lengths intimates the preservation of the building unit regardless of their different numbers of defects. As one node consists of 6 Zr and 12 carboxylate ligands, the contributed 14% of Zr(1) in the whole system of UiO-66 reflects the 0.84 defective Zr per node (0.42 missing carboxylate ligand). While, only 9% of Zr(1) corresponding to 0.54 defective Zr per node (0.27 missing carboxylate ligand) is observed in UiO-66(AA). However, if the modulator removal of UiO-66(AA) was employed (UiO-66(AA)*), the catalyst provided defective site up to 24% corresponded to 1.44 defective Zr per node.

Table S7. Zr K-edge EXAFS fitting data of UiO-66, UiO-66(AA), and UiO-66(AA)*

	Path	N	Contribution	R (Å)	10^2 x σ^2 (Å^2)	$\mathbf{S_0^2}$	ΔE (eV)	R-factor
UiO-66	Zr–O$_{\mu3}$	4	100%	2.13±0.01	0.42±0.22	1.12±0.08	7.03±0.08	0.03%
	Zr(1)–O$_{OH/H2O}$	1	14%	2.39±0.99	0.27±0.47			
	Zr(1)–O$_{COO}$	3	14%	2.28±0.01				
	Zr(2)–O$_{COO}$	4	86%					
	Zr(1)–C	3	14%	3.71±0.11	2.24±1.65			
	Zr(2)–C	4	86%					
	Zr–Zr	4	100%	3.52±0.01	0.66±0.06			
	Zr–Oc	4	100%	3.92±0.07	1.18±0.75			
	Zr–O$_{\mu3}$	4	100%	4.25±0.05				
UiO-66(AA)	Path	N	Contribution	R (Å)	σ^2 x10^2 (Å^2)	$\mathbf{S_0^2}$	ΔE(eV)	R-factor
	Zr–O$_{\mu3}$	4	100%	2.11±0.01	0.51±0.20	0.98±0.10	6.45±0.92	0.04%
	Zr(1)–O$_{OH/H2O}$	1	9%	2.75±0.06	0.44±0.16			
	Zr(1)–O$_{COO}$	3	9%	2.27±0.01				
	Zr(2)–O$_{COO}$	4	91%					
	Zr(1)–C	3	9%	3.22±0.08	1.64±1.68			
	Zr(2)–C	4	91%					
	Zr–Zr	4	100%	3.52±0.01	0.45±0.06			
	Zr–Oc	4	100%	3.49±0.12	2.39±1.98			
	Zr–O$_{\mu3}$	4	100%	4.32±0.11				
UiO-66(AA)*	Path	N	Contribution	R (Å)	σ^2 x10^2 (Å^2)	$\mathbf{S_0^2}$	ΔE(eV)	R-factor
	Zr–O$_{\mu3}$	4	100%	2.09±0.02	0.21±0.22	0.83±0.24	2.38±2.04	0.15%
	Zr(1)–O$_{OH/H2O}$	1	24%	2.69±0.47	0.03±0.22			
	Zr(1)–O$_{COO}$	3	24%	2.24±0.02				
	Zr(2)–O$_{COO}$	4	76%					
	Zr(1)–C	3	24%	2.75±0.12	0.87±0.90			
	Zr(2)–C	4	76%					
	Zr–Zr	4	100%	3.50±0.01	0.50±0.12			
	Zr–Oc	4	100%	3.47±0.03	0.71±0.67			
	Zr–O$_{\mu3}$	4	100%	3.81±0.05				

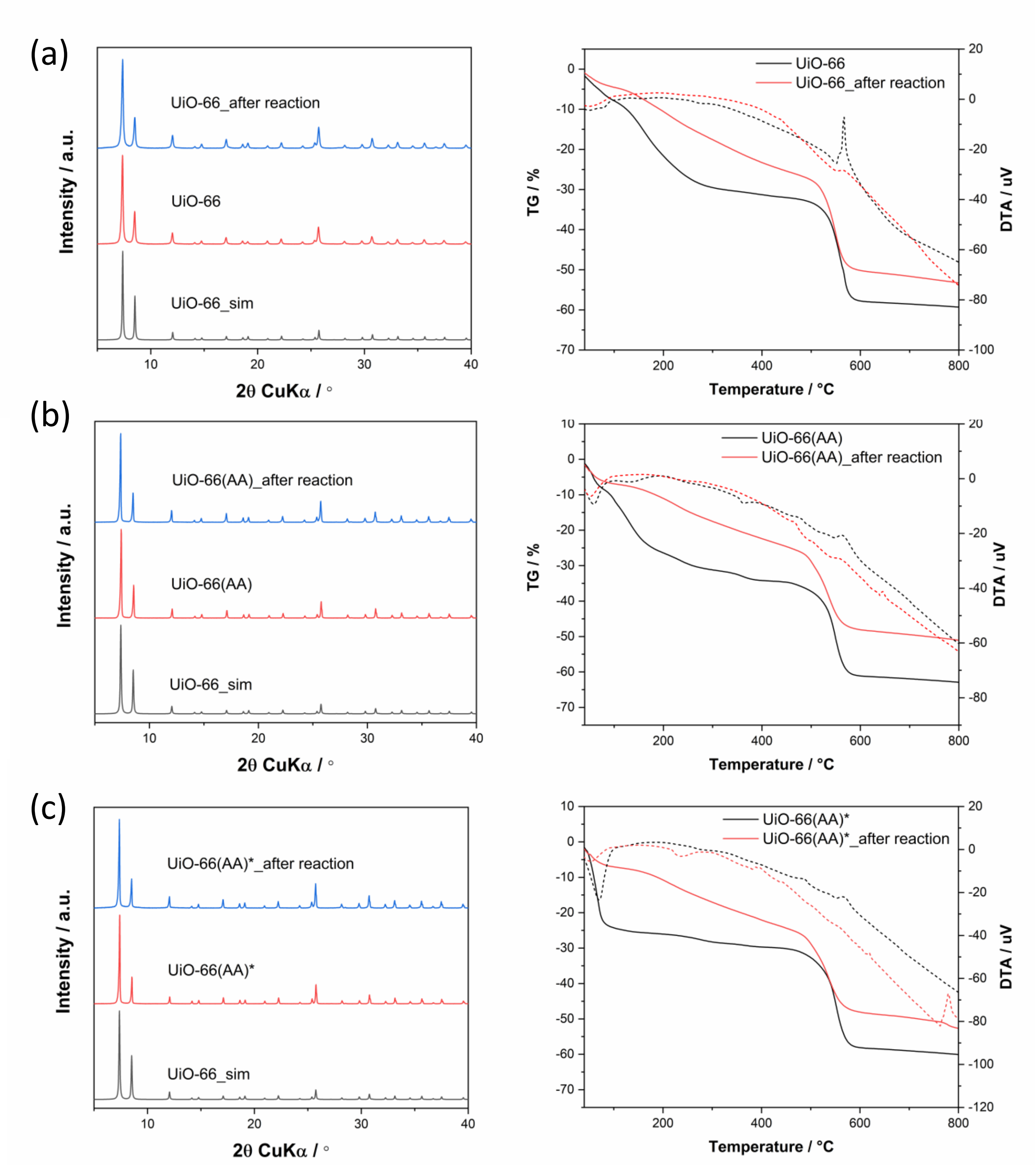

Figure S10. PXRD patterns and TGA curves of (a) UiO-66, (b) UiO-66(AA), (c) UiO-66(AA)* before and after D-xylose conversion reaction.

: PXRD patterns of all catalysts remain unchanged suggesting stability of the catalyst for LA production under hydrothermal reaction. The differences in weight loss of used catalysts after the reaction indicate the formation of humin residues.

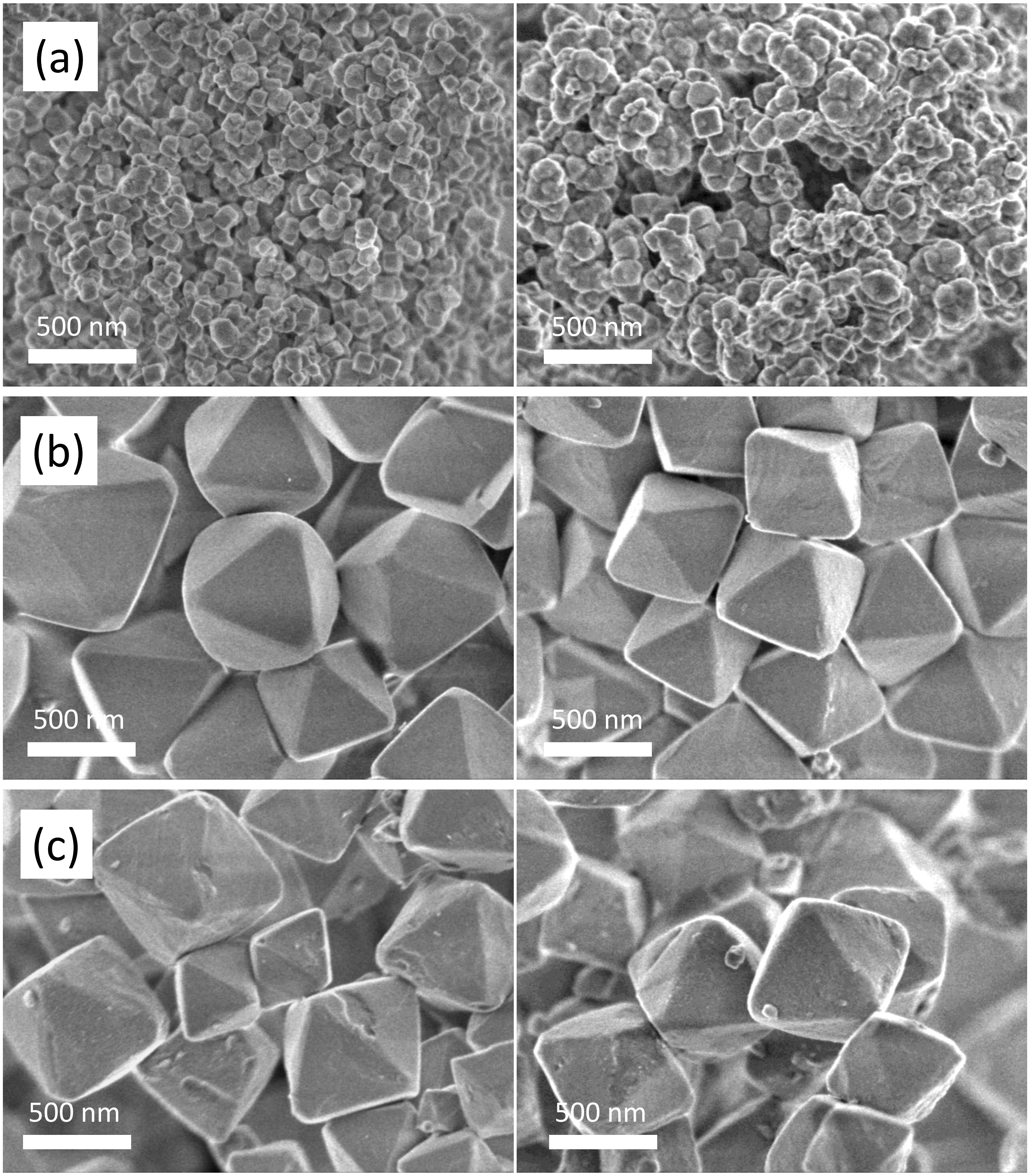

Figure S11. SEM images of (a) UiO-66, (b) UiO-66(AA), and (c) UiO-66(AA)* before and after D-xylose conversion reaction, respectively.

: The morphologies of catalysts do not change after the reaction suggesting their stabilities toward LA production by hydrothermal condition.

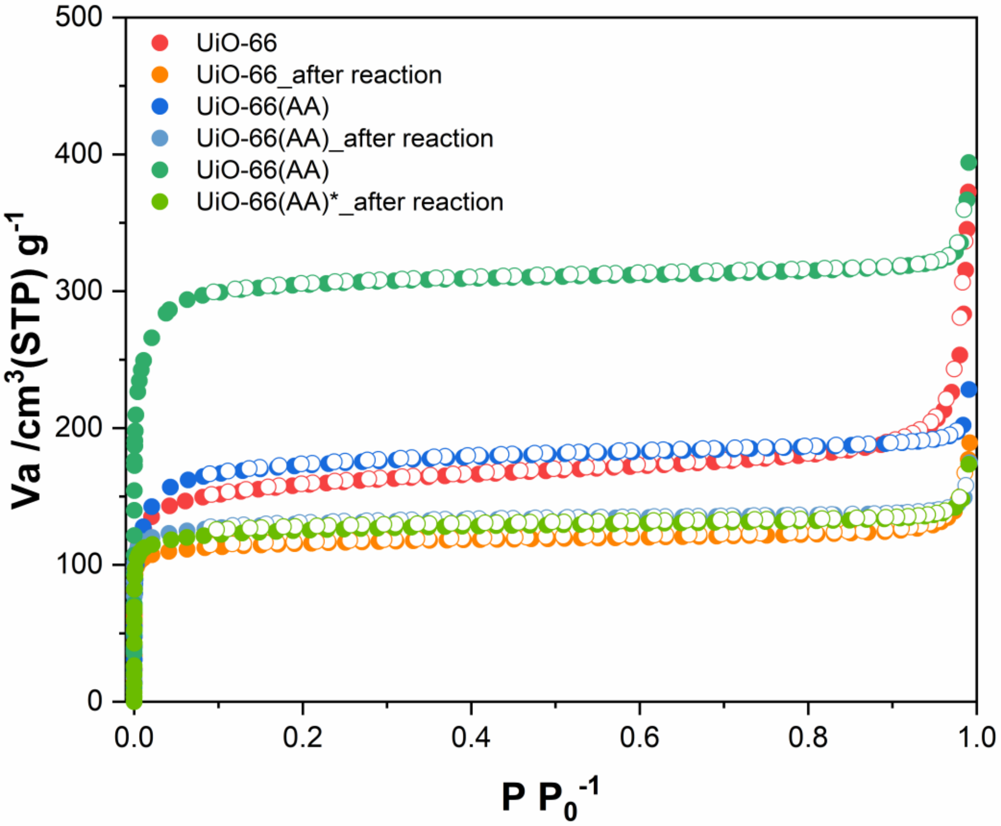

Figure S12. N_2 sorption isotherms of UiO-66, UiO-66(AA), and UiO-66(AA)* before and after the reaction. Filled and opened circles represent adsorption and desorption, respectively.

: The significant reduction of BET surface area and accessible pore volume is attributed to the presence of humin residues in the used catalysts.

Table S8. Summary of N_2 sorption capacities of the UiO-66, UiO-66(AA), and UiO-66(AA)* before and after the D-xylose conversion reaction.

Sample	Specific surface area (m^2 g^{-1})	Micropore volume (cm^3 g^{-1})
UiO-66	601.17	0.2264
UiO-66_after reaction	458.70	0.1602
UiO-66(AA)	669.71	0.2614
UiO-66(AA)_after reaction	513.36	0.1947
UiO-66(AA)*	1,198.80	0.4642
UiO-66(AA)*_after reaction	492.21	0.1867

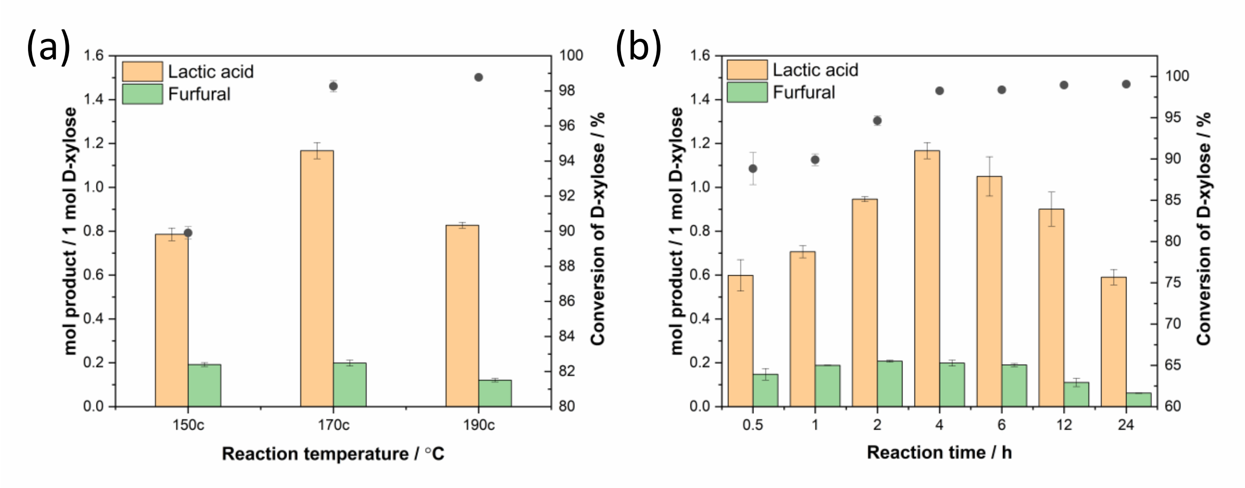

Figure S13. Effect of (a) reaction time and (b) reaction temperature on the conversion of D-xylose over UiO-66 catalyst in aqueous solution.

Hydrothermal conversion of D-xylose to LA with UiO-66 – effect of reaction temperature and reaction time on LA yield

To optimize the operating temperature on D-xylose conversion, the reactions were performed at various temperatures (150, 170, and 190 °C). At these temperatures, the coordinated water molecules can leave the defective Zr, resulting in the accessible Lewis acid sites to occur the reaction. Figure S13 compares the conversion and yields of major products (LA, formic acid, and furfural). The conversion of D-xylose is effective showing 88.90%, 98.26%, and 98.77% at the reaction temperatures of 150, 170, and 190 °C, respectively. Despite the maximum D-xylose conversion at 190 °C, the maximum LA yield of 1.17 mol is achieved at 170 °C. Based on the molar basis, the produced LA yield of 1.17 mol is slightly higher than that of the initial D-xylose reactant (1 mol). This suggests that the contribution of alternative pathways for LA production from the residues, such as C1 and C2 could be possible.[8] However, it is beyond the scope of the current study which highlights only the formation of LA from D-xylose. The insight into the possible pathways taken place is still of interest for further investigation. The lower LA yields of 0.79 and 0.83 mol are produced at 150 °C and 190 °C, respectively. According to the high temperature of the reaction at 190 °C, the products are further converted into humin. Note that, 0.20 mol of furfural occurs at 170 °C according to the competitive cyclodehydration reaction. Considering the degree of conversion, desired LA yield and unfavorable reactions, the reaction temperature of 170 °C was selected to further optimize the reaction time on D-xylose conversion.

Herein, a variation of reaction times ranging from 0.5, 2, 4, 6, 12, and 24 h was carried out. The D-xylose conversion markedly increases up to 98.26% at 4 h. Further prolongation of reaction time till 24 h reveals less effectiveness of D-xylose conversion. Conducting the reaction at 170 °C for 4 h leads to the maximum LA yield of 1.17 mol and comparable undesired furfural with the less reaction time. Extending reaction time to 6 and 12 h decreases the LA yield to be 1.05 and 0.90 mol respectively. With excessively extended reaction time to 24 h, LA yield drastically decreases to 0.59 mol. This is possibly attributed to the decomposition of LA at the prolonged reaction time. Not only the higher yield of LA but also the suppression of the formation of unfavorable furfural product which is signified as the selectivity of LA over furfural is concerned. Based on the optimal compensation of the high LA yield and the acceptable selectivity, the reaction time of 4 h was selected.

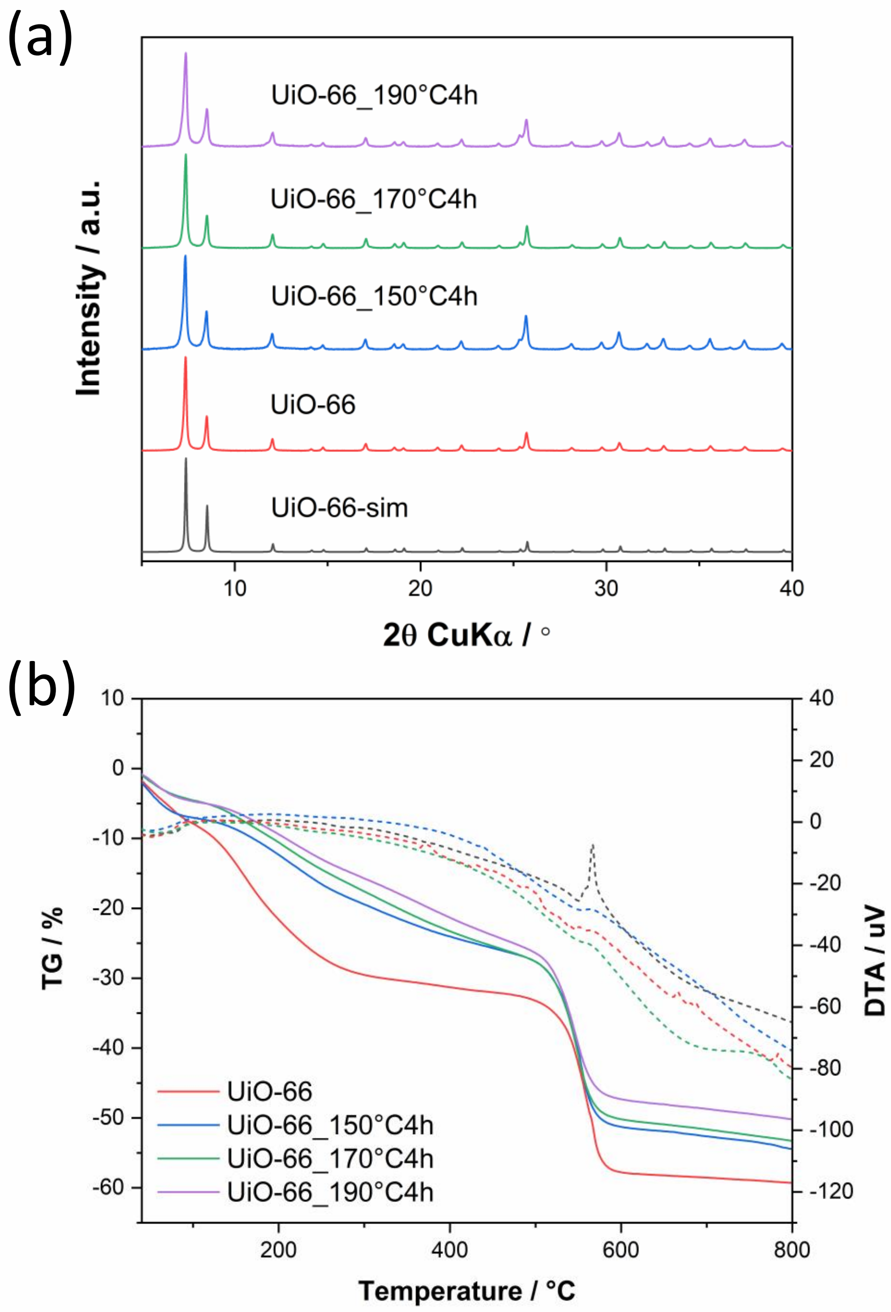

Figure S14. PXRD patterns and TGA curves of UiO-66 after D-xylose conversion reactions at various temperatures

: As evidenced by the PXRD patterns, UiO-66 catalyst could maintain its crystalline structure at the reaction from 170 °C to 190 °C. The greater differences in weight loss of catalyst after the reaction at 190 °C than 150 °C indicate that the formation of humin could be induced by the increased reaction temperature.

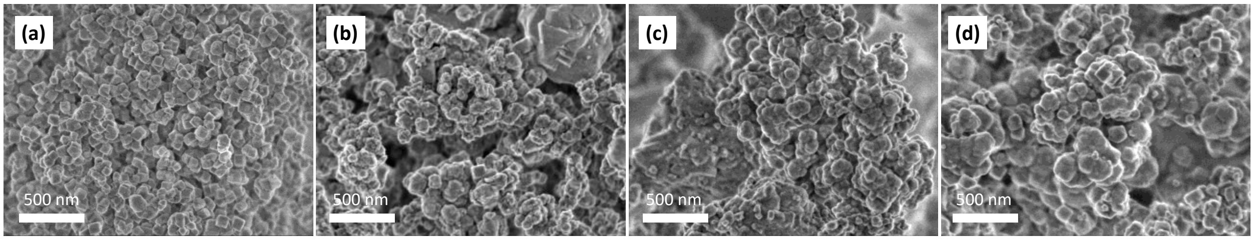

Figure S15. SEM images of (a) as-synthesized UiO-66 and UiO-66 after the reaction for (b) 150 °C-4h, (c) 170 °C-4h and (d) 190 °C-4h, respectively.

: Reaction temperature clearly affects on the morphology of UiO-66 catalyst. The reaction at 190 °C shows more coagulation of particles than those of 170 °C and 150 °C, confirming the humin formation at high temperature.

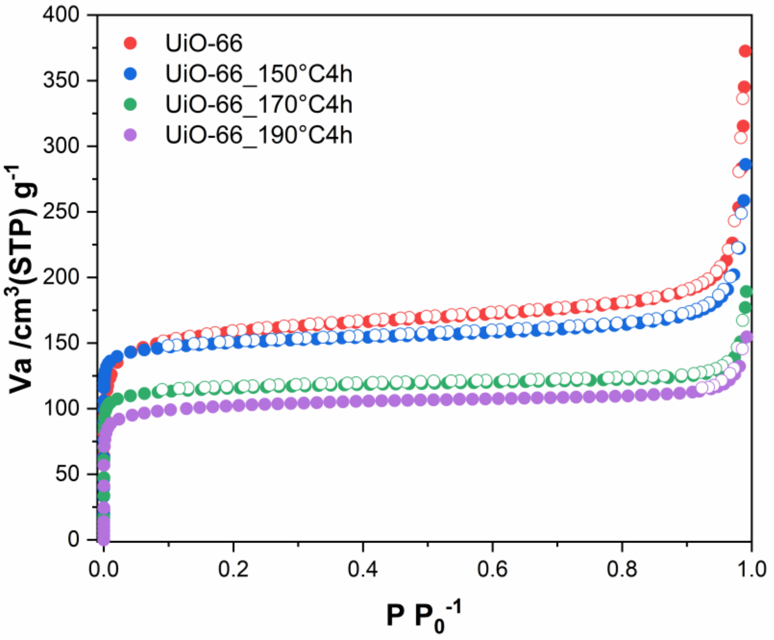

Figure S16. N_2 sorption isotherms of as-synthesized UiO-66 and UiO-66 after the reaction for 150 °C-4h, 170 °C-4h and 190 °C-4h, respectively. Filled and opened circles represent adsorption and desorption, respectively.

: The significant reduction of BET surface area and accessible pore volume is attributed to the humins formation by hydrothermal reaction at high temperature.

Table S9. Summary of N_2 sorption capacities of the as-synthesized UiO-66 catalysts after the reaction at various temperatures.

Sample	Specific surface area (m^2 g^{-1})	Micropore volume (cm^3 g^{-1})
UiO-66	601.17	0.2264
UiO-66_150°C-4h	596.51	0.2186
UiO-66_170°C-4h	458.70	0.1602
UiO-66_190°C-4h	395.27	0.1494

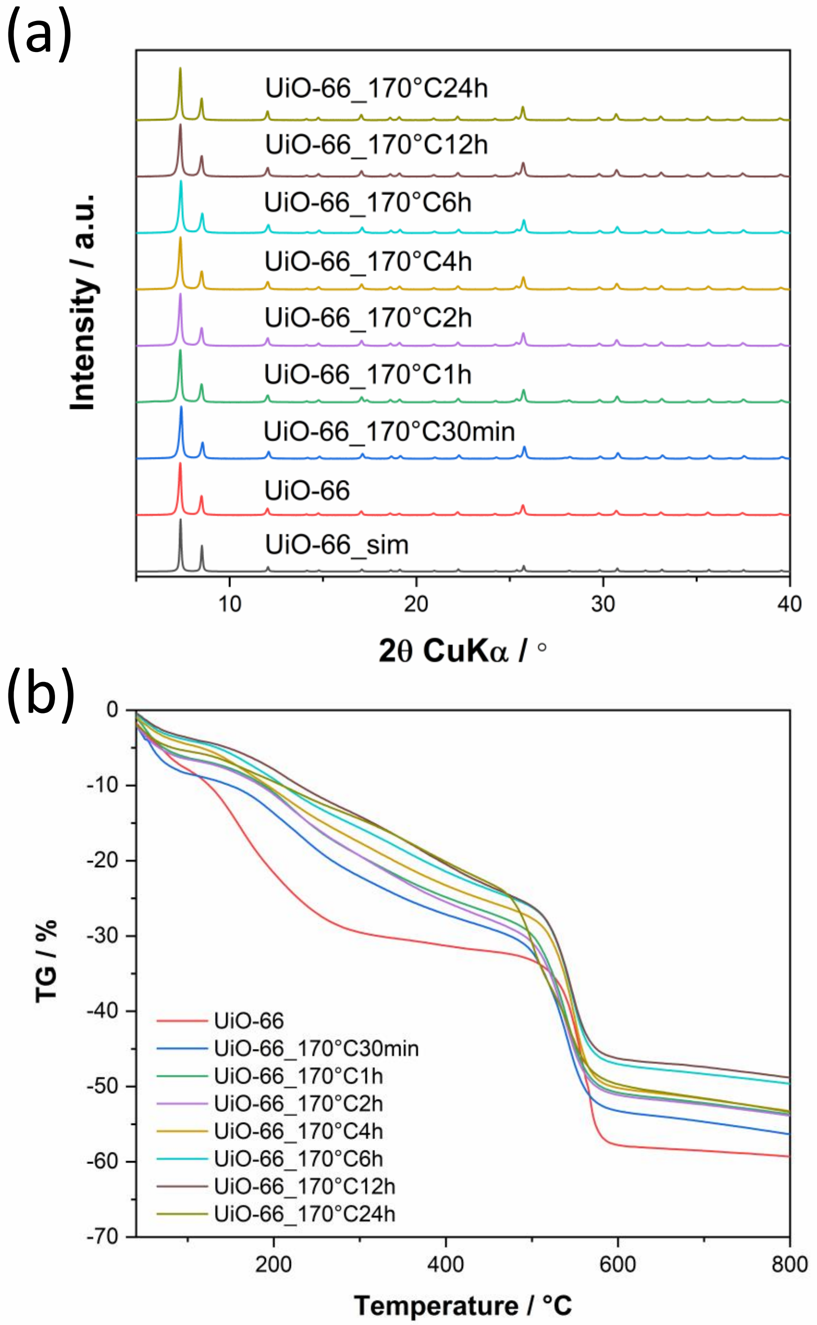

Figure S17. PXRD patterns and TGA curves of UiO-66 after D-xylose conversion at various reaction times.

: UiO-66 catalyst could maintain its crystalline structure toward the reaction at 170 °C for 30 min to 24 h. The TGA profiles show that the differences of weight loss after the reaction is increased by reaction time, suggesting the formation of humin residues in UiO-66 catalysts.

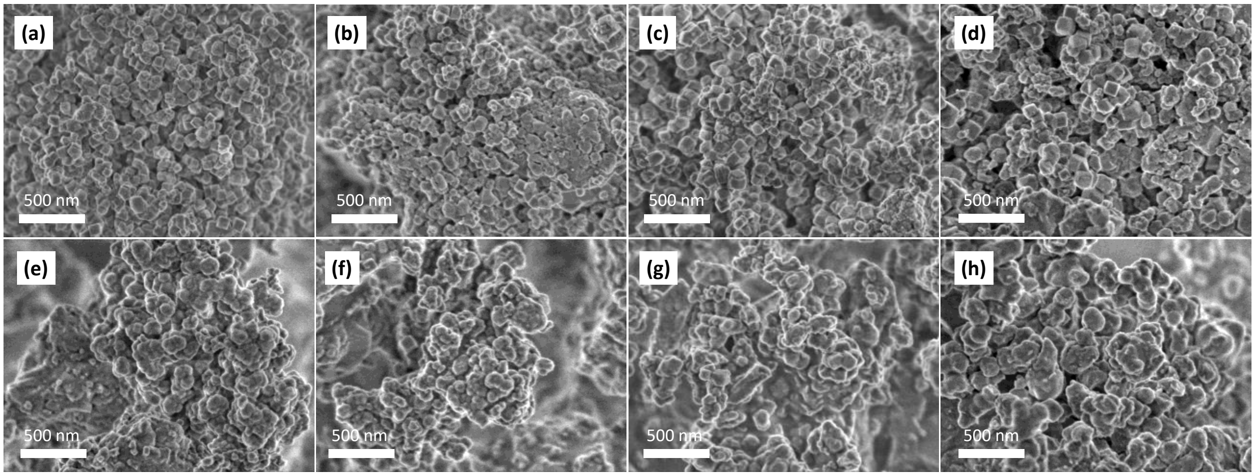

Figure S18. SEM images of (a) as-synthesized UiO-66 and UiO-66 after the reaction for (b) 0.5 h, (c) 1 h, (d) 2 h, (e) 4 h, (f) 6 h, (g) 12 h, and (h) 24 h, respectively.

: The coagulation of particles contributed to humin residues increase with reaction time.

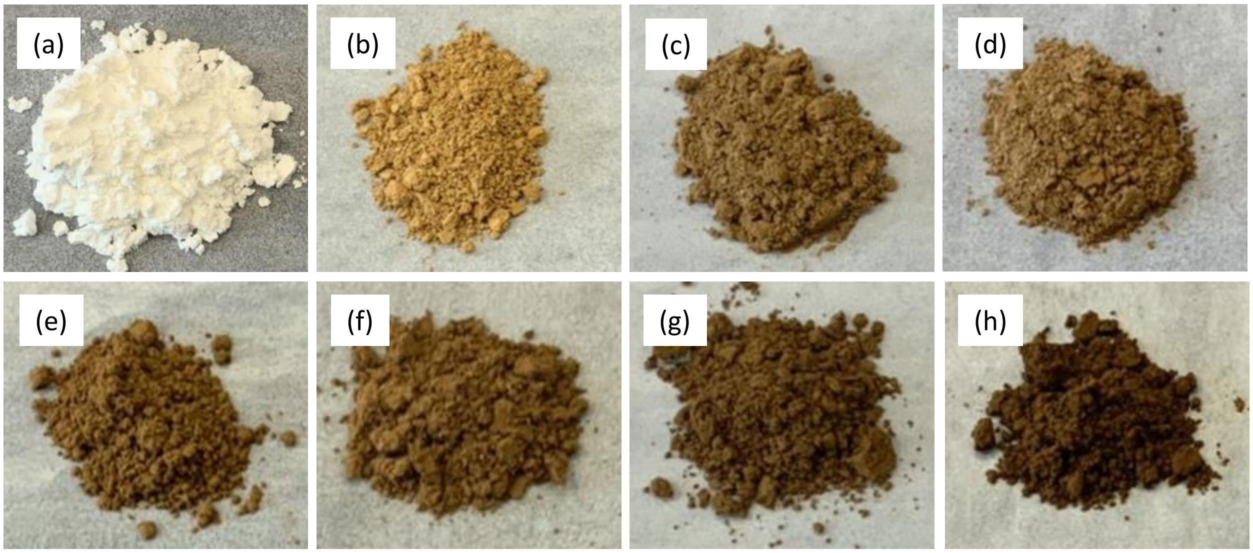

Figure S19. Powders of (a) as-synthesized UiO-66 and UiO-66 after the reaction for (b) 0.5 h, (c) 1 h, (d) 2 h, (e) 4 h, (f) 6 h, (g) 12 h, and (h) 24 h, respectively.

: The brown color of used catalysts is due to the existence of humin residues.

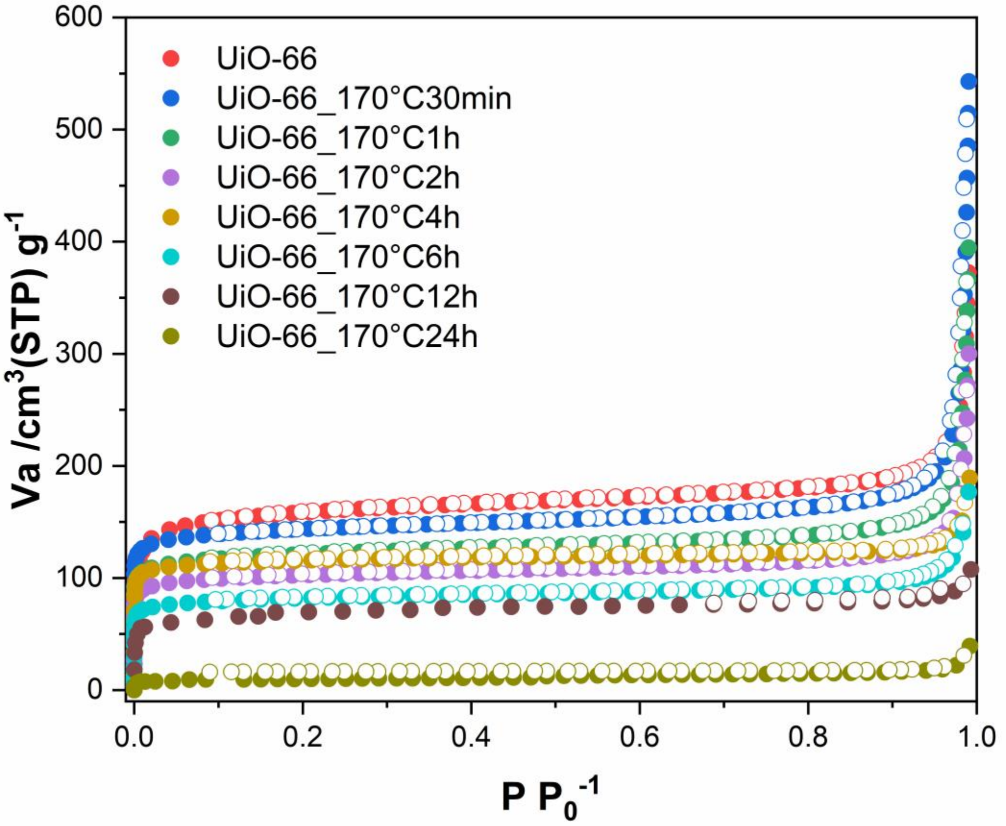

Figure S20. N_2 sorption isotherms of as-synthesized UiO-66 and UiO-66 after the reaction for 0.5, 1, 2, 4, 6, 12, and 24 h, respectively. Filled and opened circles represent adsorption and desorption.

: The sorption capacity of UiO-66 catalyst decreases with prolonged reaction time, suggesting the formation of humin residues.

Table S10. Summary of N_2 sorption capacities of the as-synthesized UiO-66 catalysts after the reaction at various times.

Sample	Specific surface area ($m^2 g^{-1}$)	Micropore volume ($cm^3 g^{-1}$)
UiO-66	601.17	0.2264
UiO-66_170 °C-30min	559.77	0.2009
UiO-66_170 °C-1h	468.37	0.1702
UiO-66_170 °C-2h	397.88	0.1467
UiO-66_170 °C-4h	458.70	0.1602
UiO-66_170 °C-6h	317.98	0.1154
UiO-66_170 °C-12h	247.67	0.1109
UiO-66_170 °C-24h	33.96	0.0125

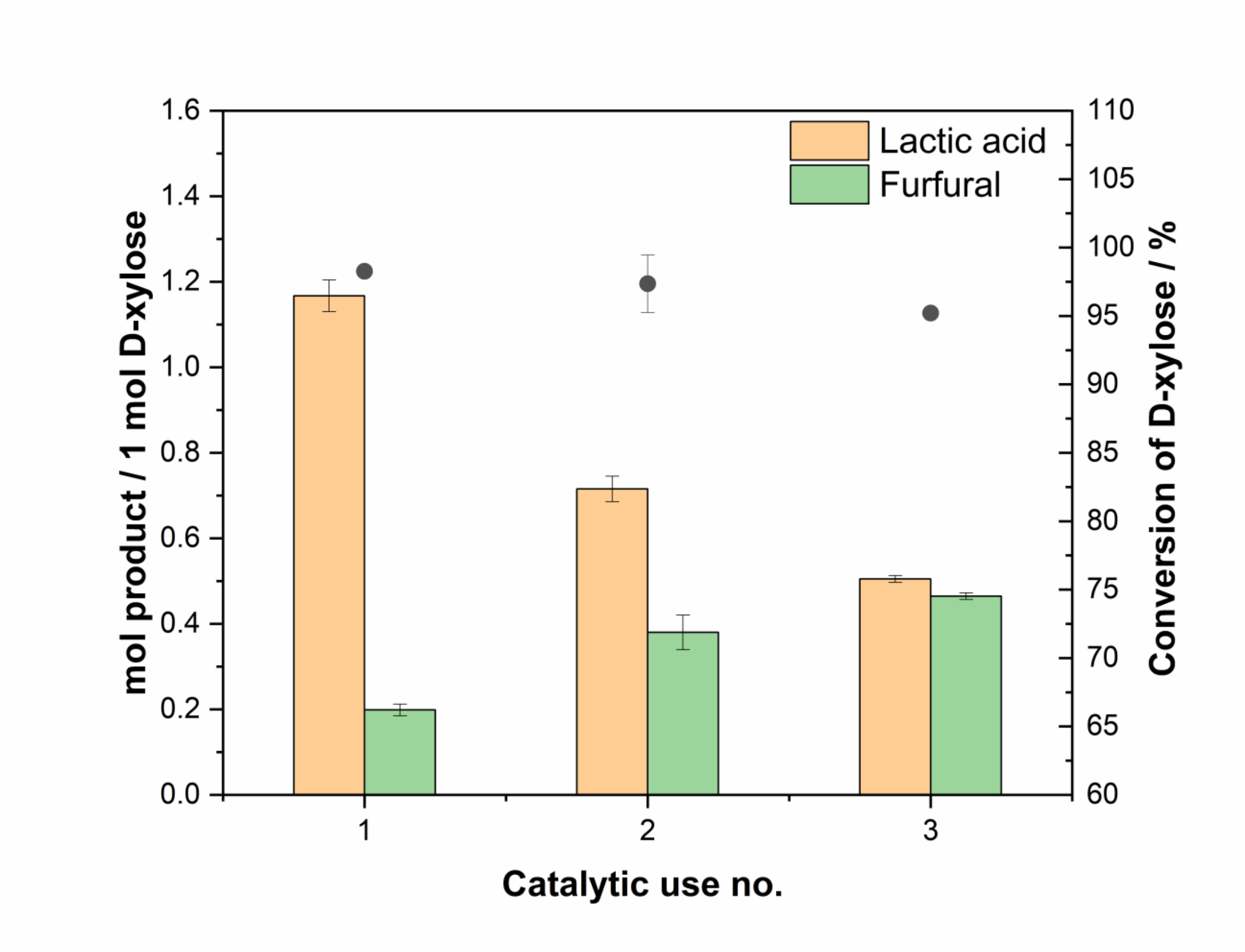

Figure S21. Catalytic performance and reusability of UiO-66 catalyst for the conversion of D-xylose in aqueous solution at 170 °C for 4h.

: The catalyst recycling experiments were performed without the regeneration at extreme condition and the results are summarized in Table S4. After drying the used UiO-66 catalyst at 80 °C under vacuum, the catalysts provide the D-xylose conversion of 98.26%, 97.35% and 95.22% with LA yield of 1.17, 0.72 and 0.50 mol for the first, second and third cycles, respectively. Although the degree of D-xylose conversions of all cycles are comparable, the LA yield observably decreases while the furfural yield is opposite with respect to the numbers of cycle. This result indicates that the presence of humin within the pores of the UiO-66 catalyst after the reaction leads to less accessibility toward the defective Zr active sites. Therefore, the used UiO-66 catalysts without regeneration reveal less efficiency for the conversion of D-xylose to LA (which requires the active sites within the pores), instead, more pronounced conversion of D-xylose to furfural (which can occur outside the pores of catalysts). Noteworthy, the regeneration process that removes the organic residues without destroying the active sites is recommended for the effective reusability of the UiO-66 catalyst.

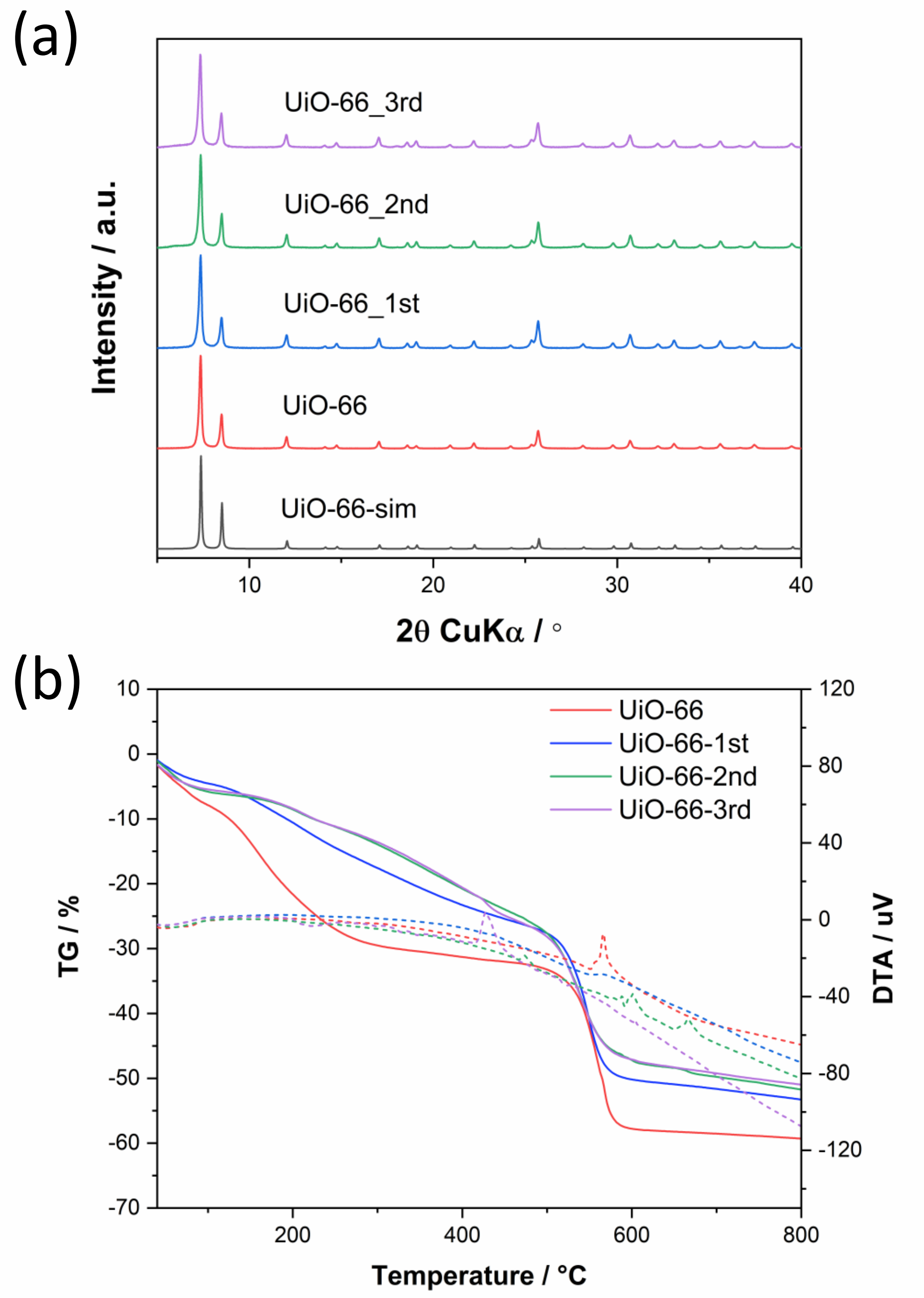

Figure S22. PXRD patterns and TGA curves of UiO-66 catalyst before and after D-xylose conversion reaction for 3 cycles.

: Maintained phase of UiO-66 catalyst shows the structural stability upon the recyclability.

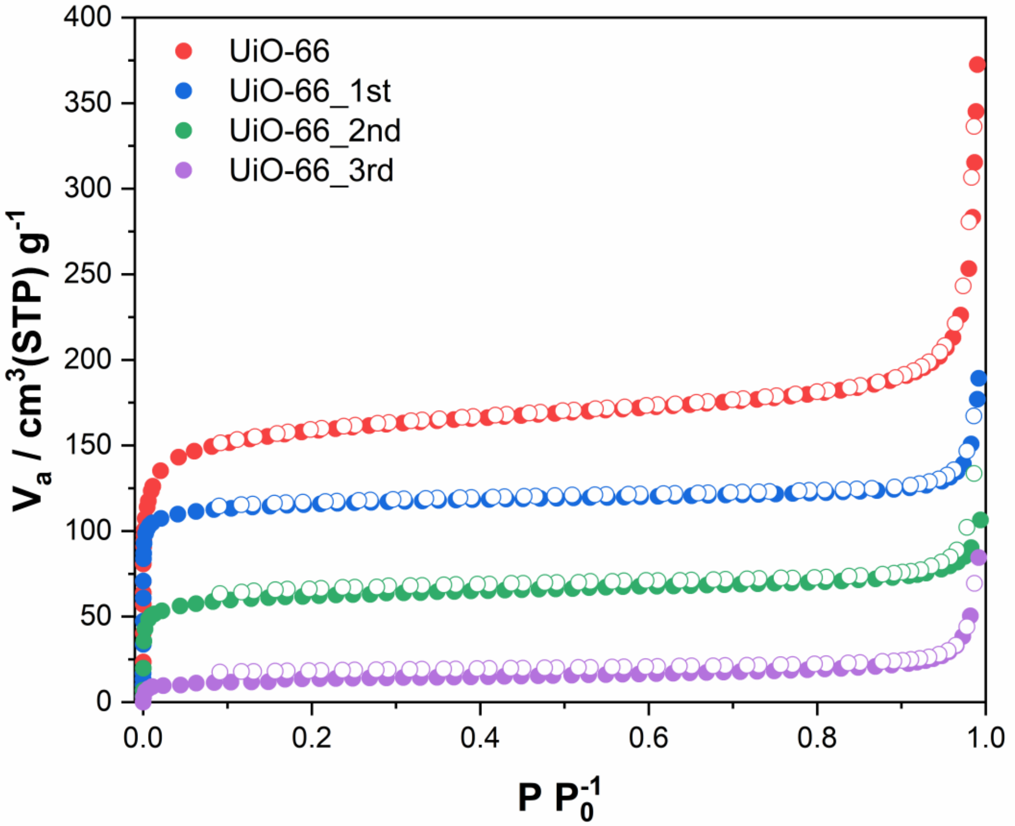

Figure S23. N_2 sorption isotherms of reused UiO-66 catalyst after D-xylose conversion reaction. Filled and opened circles represent adsorption and desorption, respectively.

: The reduction in surface area and pore volume suggest less active sites of catalyst for the reaction at more cycles.

Table S11. Summary of N_2 sorption capacities of the as-synthesized UiO-66 and UiO-66 after the reaction for 3 cycles.

Sample	Specific surface area (m^2 g^{-1})	Micropore volume (cm^3 g^{-1})
UiO-66	601.17	0.2264
UiO-66_1st cycle	458.70	0.1602
UiO-66_2nd cycle	235.41	0.0855
UiO-66_3rd cycle	47.18	0.0140

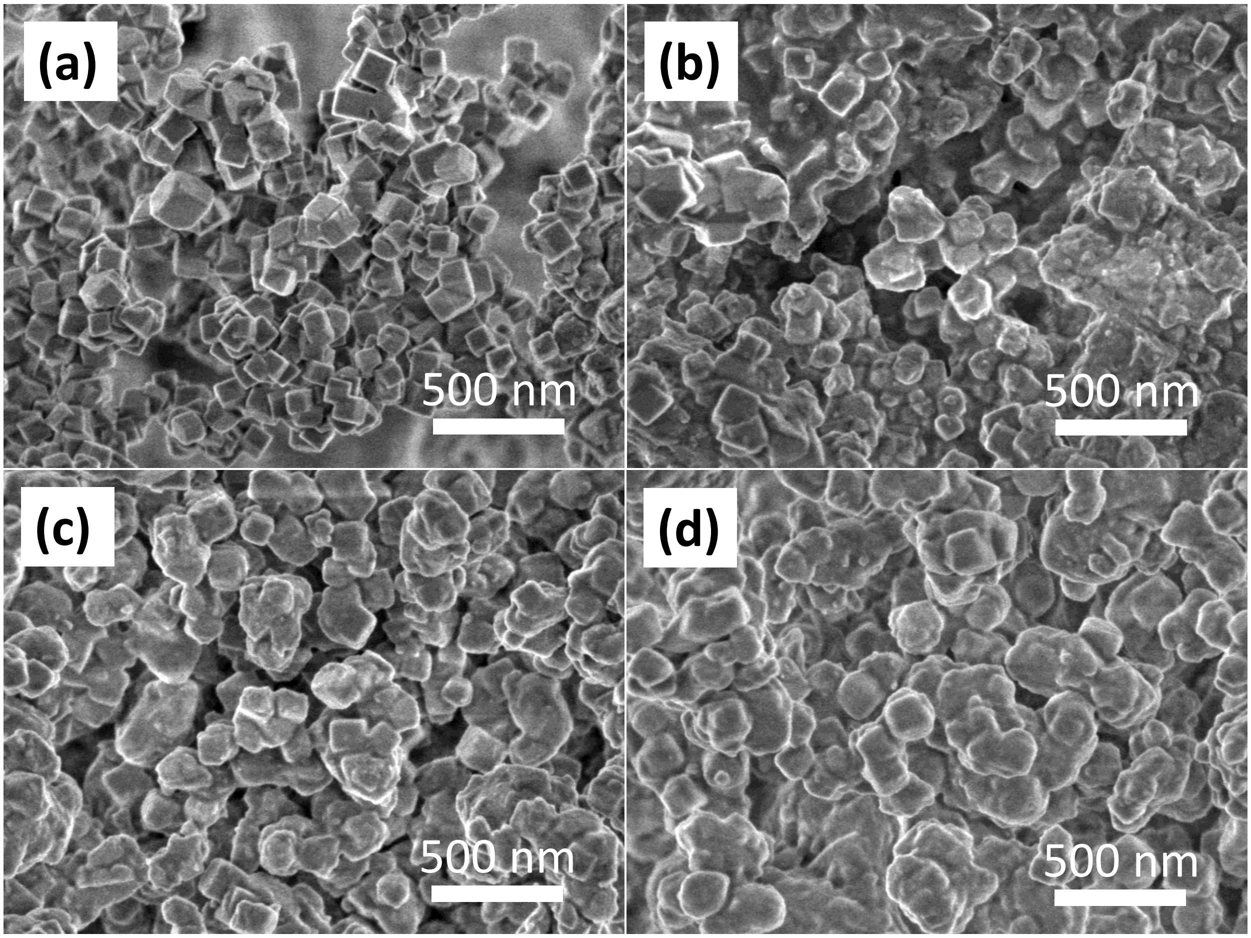

Figure S24. SEM images of (a) as-synthesized UiO-66, and UiO-66 catalyst after (b) the 1st cycle (c) the 2nd cycle and (d) the 3rd cycle, respectively.

: More coagulation of particles at the 3rd cycle than that of the 2nd and 1st cycle suggests the humin formation upon the recyclability.

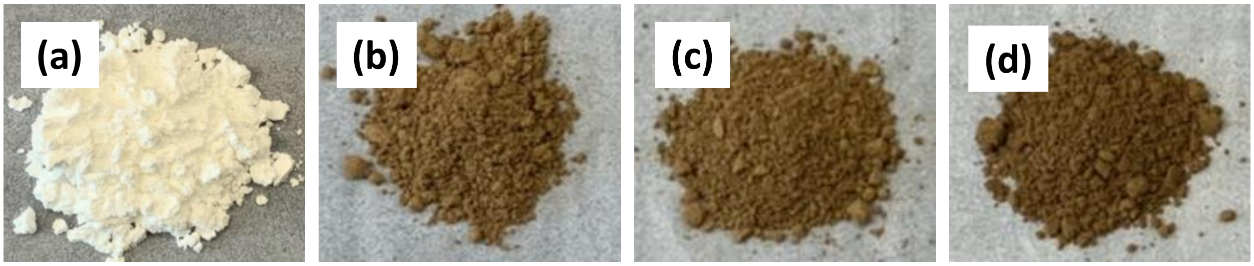

Figure S25. Powders of (a) as-synthesized UiO-66, and UiO-66 catalyst after (b) 1st cycle, (c) 2nd cycle and (d) 3rd cycle, respectively.

: The brown color of used catalysts is due to the existence of humin residue.

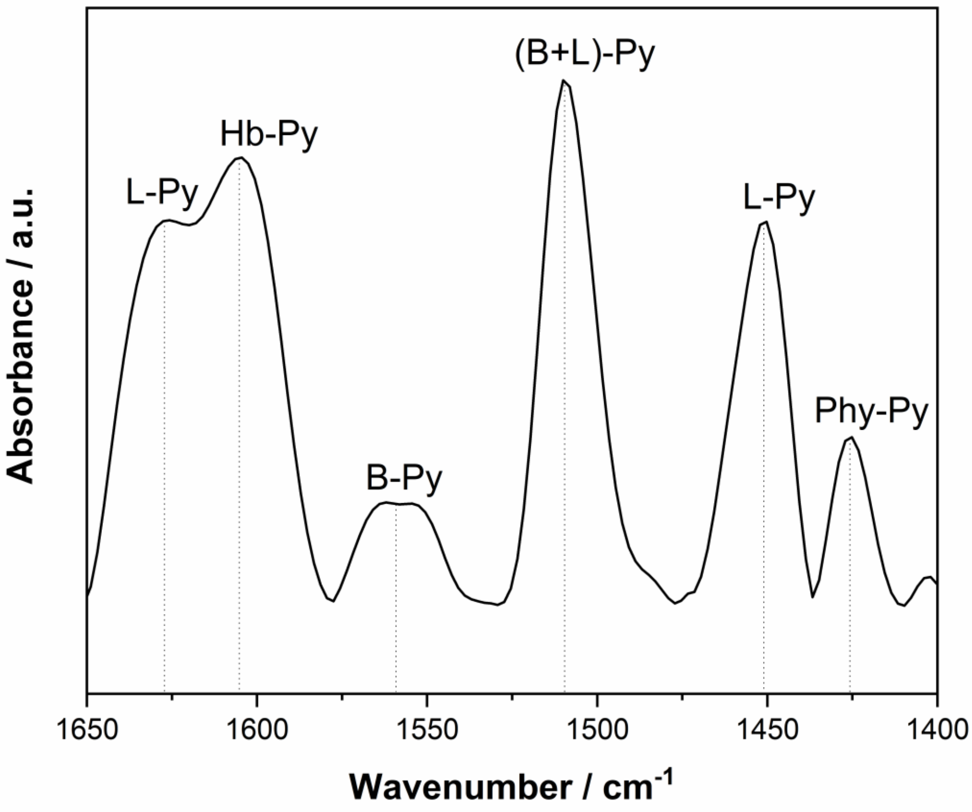

Figure S26. DRIFT spectrum of pyridine treated UiO-66(AA)* catalysts.

: The presence of Lewis and Brønsted acid sites in UiO-66(AA)* catalyst is confirmed by pyridine FT-IR. The spectrum displays a strong peak at 1450 cm^{-1} for pyridine on Lewis acid site (denoted as L–Py).[9] A band at 1509 cm^{-1} was assigned to the combination of Lewis and Brønsted sites (denoted as (B+L)–Py). The UiO-66(AA)* displays a slight peak at 1559 cm^{-1} attributed to Brønsted acid site (denoted as B–Py).

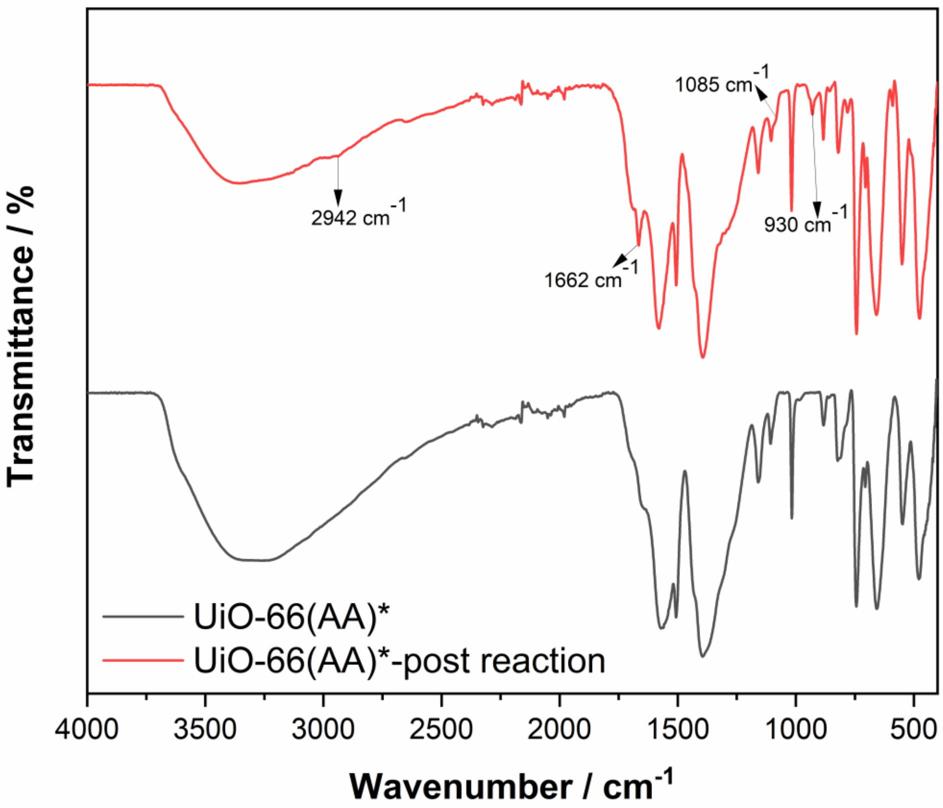

Figure S27. FT-IR spectra of UiO-66(AA)* and UiO-66(AA)* after the reaction.

: Some differences between the spectra of the fresh and used catalysts might be attributed to the existence of furan rings of humin, such as C=O stretching at 1662 cm^{-1} from conjugated ketone, C=C stretching absorption at 930 cm^{-1} and the C–O stretching absorption at 1085 cm^{-1} from primary alcohol. Additionally, a weak absorption band at 2942 cm^{-1} can be ascribed to aliphatic C–H stretches.

References

1. J. H. Cavka, S. Jakobsen, U. Olsbye, N. Guillou, C. Lamberti, S. Bordiga and K. P. Lillerud, *J. Am. Chem. Soc.*, 2008, **130**, 13850-13851.
2. J. Wei, N. Cheng, Z. Liang, Y. Wu, Z. Zou, Z. Zhuang and Y. Yu, *J. Mater. Chem. A*, 2018, **6**, 23336-23344.
3. B. N. Ravel, M. ATHENA, ARTEMIS, HEPHAESTUS, *J. Synchrotron Radiat.*, 2005, **12**, 537–541.
4. (a) G. W. T. M. J. Frisch, H. B. Schlegel, G. E. Scuseria, M. A. Robb, J. R. Cheeseman, G. Scalmani, V. Barone, G. A. Petersson, H. Nakatsuji, X. Li, M. Caricato, A. Marenich, J. Bloino, B. G. Janesko, R. Gomperts, B. Mennucci, H. P. Hratchian, J. V. Ortiz, A. F. Izmaylov, J. L. Sonnenberg, D. Williams-Young, F. Ding, F. Lipparini, F. Egidi, J. Goings, B. Peng, A. Petrone, T. Henderson, D. Ranasinghe, V. G. Zakrzewski, J. Gao, N. Rega, G. Zheng, W. Liang, M. Hada, M. Ehara, K. Toyota, R. Fukuda, J. Hasegawa, M. Ishida, T. Nakajima, Y. Honda, O. Kitao, H. Nakai, T. Vreven, K. Throssell, J. A. Montgomery, Jr., J. E. Peralta, F. Ogliaro, M. Bearpark, J. J. Heyd, E. Brothers, K. N. Kudin, V. N. Staroverov, T. Keith, R. Kobayashi, J. Normand, K.

Raghavachari, A. Rendell, J. C. Burant, S. S. Iyengar, J. Tomasi, M. Cossi, J. M. Millam, M. Klene, C. Adamo, R. Cammi, J. W. Ochterski, R. L. Martin, K. Morokuma, O. Farkas, J. B. Foresman, and D. J. Fox, *Journal*, 2016; (b) Y. Zhao and D. G. Truhlar, *J. Chem. Phys.*, 2006, **125**, 194101.

5. P. J. Hay and W. R. Wadt, *J. Chem. Phys.*, 1985, **82**, 270-283.

6. T. H. Dunning and P. J. Hay, in *Methods of Electronic Structure Theory*, ed. H. F. Schaefer, Springer US, Boston, MA, 1977, pp. 1-27.

7. (a) A. L. Semrau, S. Wannapaiboon, S. P. Pujari, P. Vervoorts, B. Albada, H. Zuilhof and R. A. Fischer, *Cryst. Growth Des.*, 2019, **19**, 1738-1747; (b) L. Valenzano, B. Civalleri, S. Chavan, S. Bordiga, M. H. Nilsen, S. Jakobsen, K. P. Lillerud and C. Lamberti, *Chem. Mater.*, 2011, **23**, 1700-1718; (c) Z. Su, Y. R. Miao, G. Zhang, J. T. Miller and K. S. Suslick, *Chem. Sci.*, 2017, **8**, 8004-8011.

8. H. Kishida, F. Jin, X. Yan, T. Moriya and H. Enomoto, *Carbohydr. Res.*, 2006, **341**, 2619-2623.

9. F. Wang, Z. Chen, H. Chen, T. A. Goetjen, P. Li, X. Wang, S. Alayoglu, K. Ma, Y. Chen, T. Wang, T. Islamoglu, Y. Fang, R. Q. Snurr and O. K. Farha, *ACS Appl. Mater. Interfaces*, 2019, **11**, 32090-32096.